Systematic and comprehensive comparison of two semianalytical models of microbunching instability

S. Di Mitri,[1,2,*] G. Campri,[1,3] F. Elisii,[2] G. Perosa,[4] and S. Spampinati[1]

[1]*Elettra—Sincrotrone Trieste S.C.p.A., S.S. 14 km 163,5 in Area Science Park, I-34149 Basovizza, Trieste*
[2]*Department of Physics, University of Trieste, Via Alfonso Valerio 2, I-34127 Trieste*
[3]*Department of Physics, University of Rome La Sapienza, p. le Aldo Moro 2, I-00185 Rome*
[4]*European XFEL, Holzkoppel 4, G-22869 Schenefeld*

(Received 27 November 2024; accepted 26 March 2025; published 15 April 2025)

The systematic comparison of two semianalytical models of microbunching instability affecting electron beams in single pass or recirculating linear accelerators is reported. The comparison is comprehensive of numerous features of the instability, such as low and high gain contributions, either linearized or at second order, coherent synchrotron and edge radiation, and Landau damping by transverse emittance and laser heater, investigated for single and double magnetic bunch length compression. The comparison is enriched by three different expressions—one of which is new—to calculate intrabeam scattering. The inclusion of this effect allows the recovery of agreement with published experimental observations, to date either in disagreement with theory or in partial agreement by virtue of blind fitting of parameters. The study is complemented by the evaluation of beam heating for oblique electron-laser interaction, this scheme being relevant for high repetition rate free-electron lasers, space constrained, or subject to perturbations by the laser heater chicane.

DOI: 10.1103/PhysRevAccelBeams.28.044401

I. INTRODUCTION

In single pass or recirculating electron linear accelerators (linacs), microbunching instability (MBI) is the beam collective effect causing disruption or dilution of the longitudinal phase space by the amplification of energy and density modulations in succession [1].

The instability is one of the potential showstoppers to longitudinal coherence at the Fourier limit level of linac-driven XUV free-electron lasers (FELs). In particular, it has been recognized at the origin of the radiation pedestal and power reduction in x-ray self-seeded FELs [2] and of sidebands in externally seeded EUV FELs [3,4]. In general, the instability determines FEL bandwidth enlargement and reduction of the spectral flux, in proportion to the harmonic jump of lasing.

The instability is seeded by the granularity of the electron distribution (shot noise), possibly in combination with narrowband phase space structures originated in radiofrequency (rf) photoinjectors [5,6]. The nature of the initial modulations, in combination with some damping mechanisms, commonly bounds the instability to final wavelengths in the range of ∼0.1–10 μm, hence the naming.

The first observation of the instability can be traced back to the fragmentation of the longitudinal phase space at the Tesla Test Facility in 2001 [7]. That was soon after explained as the result of the positive feedback of density and energy modulations—so-called klystron instability [8]—mediated by longitudinal space charge force (LSC, intrabunch Coulomb interaction generating density to energy conversion) [9] and particles' dispersive motion in magnetic bunch length compressors (energy to density) [10]. In the same year, a simulation study revealed the contribution to the instability of coherent synchrotron radiation (CSR) emitted in dipole magnets of the compressors [11].

The spread of particles' path length in dispersive regions, due to either chromatic or betatron motion, washes out modulations at the shortest wavelengths of the broadband instability spectrum, in fact putting in place longitudinal and transverse Landau damping [12]. Transverse damping can be enhanced by optics tuning for an enlarged curl-H_x function (see definition below) [13], while the betatron emittance is preserved. Longitudinal damping is usually more effective than the transverse. It is more effective for larger beam uncorrelated energy spread, and this is in most cases increased by a laser heater system [14] in the low energy region of the linac, well before the instability builds up. In this case, however, the enlargement of the beam longitudinal emittance imposes a trade-off between FEL spectral purity and intensity [15,16]. Additional damping

*Contact author: simone.dimitri@elettra.eu

mechanisms have been identified in the folding of phase space at high energy (phase mixing, reversible process) [17] and, recently first observed in an electron linac, intrabeam scattering (Landau damping, diffusive process) [18].

Several numerical methods and tools to simulate the instability are available to the community, see e.g. [19–25]. Particle-in-cell codes and Vlasov solvers trade off computational effort and numerical noise control. Semianalytical models offer noise-free minimal computing effort at the expense of accuracy. Still, these are essential to identify the dominant physical processes driving the instability (which can be different at different facilities). For this reason, they find application in the estimation of the spectrum of final modulations and beam energy spread during the facility design as well as for optimizing its setup during operation or in upgrade scenarios.

At least three semianalytical approaches to model MBI have been developed in the last two decades, which can be shortly referred to as, respectively, the integral linearized Vlasov-Maxwell equation [26], matrix multiplication [27], and the linearized Vlasov-Poisson equation in a plasma [28,29]. In the following, we will focus on the first two; for the sake of brevity, we will name them Huang-Kim (HK) and Bosch-Kleman-Wu (BKW), with reference to the authors who, after the conceptualization by Saldin *et al.* in [8], first introduced the formalisms with prescriptions for a numerical implementation. The models are basically time independent (they describe the bunch core slice dynamics), valid in ultrarelativistic regime, and averaging over betatron oscillations. The use of effective transverse beam sizes in the calculation of Coulomb interactions justifies 1.5-D approximations to some extent [30,31].

The HK and BKW have been independently and sparsely benchmarked with either simulations or measurements in a diversified range of accelerator parameters, often with an incomplete modeling of instability features, and rarely applied to the entire linac [23,25,27,30,32–42]. Despite the generally recognized agreement of the formalisms with simulation results, their mutual consistency has never been investigated.

The present work is the first aiming at fulfilling that task by conducting a systematic comparison comprehensive of numerous features of the instability, such as low and high gain terms, in linear and nonlinear approximation, coherent synchrotron and edge radiation, transverse and longitudinal Landau damping, investigated for one- and two-stage magnetic compression, in a range of beam and linac parameters typical of XUV FELs. In relation to the existing literature, such an extensive comparison makes a point about the state-of-the-art of the analytical computation of the instability. As a by-product of the study, the proposed implementation of HK and BKW is shown to be able to discriminate driving and negligible terms to the instability buildup as a function of the linac setup.

Two linac sets, used hereafter as case study, are summarized in Table I. The 1.5 GeV linac exemplifies FELs approaching the water window with high harmonic jumps, such as FERMI [43], SXFEL [44], and sFLASH [45]. The

TABLE I. Input parameters to model MBI in linac-FELs. BC stays for bunch compressor. The compression scheme is indicated as 1S = one-stage (single compression), 2S = two-stage (double compression).

Parameter	Seeded FEL		SASE FEL		Units
Mean energy	0.1 → 1.5		0.1 → 10		GeV
Total linac length	120		570		m
Accelerating gradient, average	∼12		∼20		MV/m
Charge	500		100		pC
Duration, FWHM	8 → 0.7		4.5 → 0.05		ps
Peak current (core)	60 → 720		20 → 1800		A
Normalized transverse emittance (round beam)	0.6		0.2		μm
Average beam radius, r_b	100 → 30		50 → 15		μm
Uncorreraled energy spread	2		1		keV
Laser heater beam energy	100				MeV
Relative energy spread at BCs	<2				%
BCs curvature radius, R	>5				m
BCs inner drift length, L	2.5				m
BCs chamber radius/height	>20				mm
BC1 beam energy	0.3				GeV
BC2 beam energy	0.7		1.5		GeV
Compression scheme	2S	1S	2S	1S	
BC1 R_{56}	40		40		mm
BC1 compression factor	4	12	15	45	
BC2 R_{56}	17	0	25		mm
BC2 compression factor	3	1	6	2	

relatively high charge and low peak current, hence long bunch duration at the undulator, reflect the need for a flattop current profile to accommodate external seeding. The 10 GeV linac suggests configurations of self-amplified spontaneous emission [46,47] in hard x-rays, such as at LCLS [48], SACLA [49], and PAL-FEL [50]. For each linac, the total bunch length compression factor is distributed with either $C_1 \gg C_2$ (hereafter, "one-stage") or $C_1 \approx C_2$ ("two-stage").

Some theoretical background on the modeling of MBI is given in Sec. II, followed by a synthetical description of our implementation of the HK and the BKW formalism, and accompanied by a quantitative discussion of approximations usually not treated in the literature. Section III starts comparing the models for the simplest picture of LSC-driven-only instability. Then, the relevance of coherent synchrotron and edge radiation, laser heater, and linear vs nonlinear gain, in light of, and in partial disagreement with, the cited literature, is discussed. The comparison is extended to three different calculations—one of which is new—of intrabeam scattering. This effect is shown in Sec. IV to recover the agreement with published experimental observations, to date either lacking a theoretical benchmark, or in disagreement with incomplete models of the instability, or in partial agreement by virtue of blind fitting of parameters. In Sec. V, the HK model is adopted to study beam heating in parallel vs oblique electron-laser interaction, the latter configuration being potentially relevant for very high repetition rate FELs, space constrained, or subject to instability development through the laser heater chicane. We reach conclusions in Sec. VI.

II. THEORETICAL FRAMEWORK

A. Impedances, gain, energy spread

We aim at describing MBI in high brightness rf linac-driven XUV FELs, where magnetic compression is implemented through (say, horizontal) four-dipole chicanes or similar first-order achromatic insertions [10].

The injected particles are assumed to be in the ultrarelativistic regime, i.e., the line-charge distribution is frozen in drift sections despite a relative longitudinal momentum spread as large as ~1%. The transverse motion is assumed to be emittance dominated, i.e., direct transverse space charge effects are neglected, owing to physical considerations such as transverse momenta much larger than the longitudinal one in the beam's reference frame, pencil-beam approximation in the laboratory frame, and high sensitivity of FELs to beam energy spread.

The effect of near and far fields of the collective bunch interaction in the regime of ultrarelativistic motion is modeled, respectively, as longitudinal space charge (LSC) and coherent synchrotron radiation (CSR) impedance per unit length, in units of Ω/m.

The LSC impedance per unit length in free space adopted hereafter is the result of averaging over a transverse round-disk uniform distribution of charges, whose area is πr_b^2 [9,51]:

$$Z_{\mathrm{LSC}}(k) = \frac{iZ_0}{k\pi r_b^2}\left[1 - 2I_1\left(\frac{kr_b}{\gamma}\right)K_1\left(\frac{kr_b}{\gamma}\right)\right], \quad (1)$$

where $Z_0 = 376.73\ \Omega$, $I_A = 17045$ A, I_1, K_1 are modified Bessel functions of the first kind, γ is the relativistic Lorentz factor for the beam mean energy, and $k = 2\pi/\lambda$ is the modulation wave number. The effective radius $r_b = 0.8735(\sigma_x + \sigma_y)$, with $\sigma_{x,y}$ the standard deviation of a bidimensional Gaussian distribution, is introduced to match well-established 3D simulation results by space-charge codes [31,51]. Equation (1) is shown in [52] to be valid for any beam transverse aspect ratio $0 < \sigma_y/\sigma_x < 1$. However, it is noteworthy that the model does not work well at high frequencies or $k\sigma_{x,y}/\gamma \gg 1$ [31].

Expressions similar to Eq. (1) exist for Z_{LSC} in the presence of round or rectangular vacuum chamber [53], whose shielding effect can nevertheless be neglected as long as $kr_c/\gamma \geq 1$ and $r_b/h_c \ll 1$, with r_c and h_c the vacuum chamber radius and height, respectively. These conditions are both satisfied for the ranges of interest in Table I and modulation wavelength of $\lambda \leq 100\,\mu\mathrm{m}$.

Equation (1) describes the longitudinal force internal to a bunched beam whose longitudinal slices are transversally aligned in a drift section. The assumption is approximately satisfied in magnetic compressors, where, for typical linear energy chirp $h \approx \sigma_{\delta,\mathrm{cor}}/\sigma_z \leq 20\ \mathrm{m}^{-1}$, betatron beam size $\sigma_{x,\beta} \approx r_b$, and dispersion function $\eta_x \approx R_{56}R/L_d \leq 0.1$ m (R bending radius, L_d dipole length), any central slice of length $\sigma_{z,sl} \leq \sigma_z/100 \approx 10\,\mu\mathrm{m}$ is misaligned with respect to adjacent ones because of the chromatic motion by no more than $\Delta x_\eta/\sigma_{x,\beta} \approx 0.5 \times \eta_x h\sigma_{z,sl}/\sigma_{x,\beta} \approx 20\%$ of its intrinsic size. Despite the overall compressors' length being a small portion (< 5%) of the total length of the accelerator, the proposed implementation of both HK and BKW takes into account the LSC effect along the compressors.

CSR in magnetic compressors is essentially THz radiation emitted by bunches of sub-mm length. It is described by the free-space 1D steady state impedance per unit length [54]:

$$Z_{\mathrm{CSR}}(k) = (1.63 + i0.94)\frac{Z_0}{4\pi}\frac{k^{1/3}}{|R|^{2/3}}. \quad (2)$$

Vacuum chamber shielding [55,56] can be neglected as long as $\sigma_z < (\pi\sqrt{R/(2h_c)^3})^{-1} \approx 1.5$ mm for the parameters in Table I, which is, therefore, the case for the bunch lengths under consideration. According to theory in [57], the 1D approximation of Eq. (2) is valid as long as the so-called Derbenev's criterion is satisfied, i.e., $\sigma_{\mathrm{DC}} = \sigma_{x,y}/(\sigma_z^{2/3}R^{1/3}) \ll 1$. However, a recent comparison of predictions of projected emittance growth by 1D CSR analytical model, tracking codes and experimental data [58]

suggest that, in fact, the Derbenev criterion can be relaxed; namely, 1D analytical and numerical models well reflect the measured data up to $\sigma_{\mathrm{DC}} \approx 2$ or so. According to these observations, Eq. (2) is expected to be valid up to quasifull compression, i.e., for beams whose longitudinal phase space is close to, but not fully, upright.

Equation (2) does not take into account the transient CSR field at the dipole edges [59] and CSR field propagating in downstream drifts [60]. Simulation results in [61] for a multibend arc compressor suggest that the relative magnitude of their contribution to the change of particles' momentum, scaled to a four-dipole compressor and for beam parameters in the range of Table I, is $\sim O(10\%)$. Analytical and numerical results in [62] for four-dipole chicanes reinforce that expectation: the CSR-only contribution to the instability gain is $\sim O(10)$ at maximum, no more than 25% of which is due to transient effects, and, as shown below, 1 to 2 orders of magnitude smaller than the gain driven by LSC.

Nevertheless, the CSR exit-transient field, which is shown in [62] to be the most relevant contribution among all nonsteady ones, is modeled as 1D coherent edge radiation (CER) impedance integrated over a drift of length L downstream the magnet, in units of Ω [63]:

$$\int_0^L Z_{\mathrm{CER}}(k;s)ds = \frac{Z_0}{2\pi}\ln\left[\frac{\min(L,\gamma^2\lambda/2\pi)}{\lambda^{1/3}R^{2/3}}\right]. \quad (3)$$

Incoherent synchrotron radiation (ISR), whose critical frequency is in x-rays, does not contribute to the instability because of its negligible intensity ($< 10^5$-fold smaller) and smaller angular divergence (sub-mrad) compared to CSR. The dilution of transverse emittance by ISR and CSR can be taken into account through analytical estimations [64,65]. However, by virtue of ~m-level bending radius of compressors at (sub-)GeV-beam energies and well-established optics manipulation for emittance preservation, the local beam size variation due to ISR- and CSR-induced emittance growth is substantially unimportant to the calculation of Z_{LSC}.

To characterize the instability, we will refer to the spectrum of the 1D bunching factor, defined as the Fourier transform of the current modulation relative to the local smoothed "average" current I (see, e.g., [39]). The seed of the instability is assumed to be a broadband ($\Delta\lambda/\lambda \approx 1$) shot noiselike density modulation, i.e., the fluctuation of the average number of electrons per modulation period T obeys Poisson statistics. In this case, the initial bunching factor results:

$$|b_0(k)|^2 = \left|\frac{\sigma_I}{I_0}(k)\right|^2 = \left|\frac{1}{\Delta z_b}\int_{-\infty}^{+\infty}\frac{\Delta I(z)}{I_0}e^{-ikz}dz\right|^2 = \frac{1}{n_e} = \frac{1}{N_e/(\frac{\Delta t_b}{T})} = \frac{ec}{I_0\lambda} = \frac{ec}{2\pi I_0}k, \quad (4)$$

where e is the electron charge and c the speed of light in vacuum, n_e the expectation for the average number of electrons per modulation period, N_e the total number of electrons over a bunch length $\Delta z_b = c\Delta t_b$, I_0 the initial value of the local smoothed "average" current, and $\Delta I(z) = I(z) - I_0(z)$ is the fluctuation around I_0.

The spectral gain of the instability is the ratio of the final and the initial bunching factor. Its expression for the simplest configuration of LSC-dominated drift section followed by a dispersive section at constant energy well exemplifies the physics of instability growth and damping. In the approximation of a sinusoidal distortion of the energy distribution, but limited to the first harmonic of the modulation, the gain results [8,23]:

$$G^1(k;s) = \left|\frac{b_f}{b_0}\right| = \left|1 - \frac{2J_1(CkR_{56}\frac{\Delta\gamma}{\gamma})}{b_0}\right| LD_\perp LD_\parallel \cong \left|\frac{4\pi}{Z_0}\frac{I_0}{I_A}CkR_{56}\int_0^s \frac{Z_{\mathrm{LSC}}(k;s')}{\gamma(s')}ds'\right| LD_\perp LD_\parallel, \quad (5)$$

where we introduced k for the initial (uncompressed) modulation wavelength, the bunch length linear compression factor $C = (1 - hR_{56})^{-1}$, and the energy modulation amplitude induced by the collective effect *prior* to compression:

$$\frac{\Delta\gamma}{\gamma}(k;s) = -\frac{4\pi}{Z_0}\frac{I_0}{I_A}\int_0^s b(k;s')\frac{Z_{\mathrm{LSC}}(k;s')}{\gamma(s')}ds', \quad (6)$$

longitudinal and transverse Landau damping, whose effect is proportional respectively to the relative uncorrelated energy spread $\sigma_{\delta,0}$ and the geometric horizonal emittance $\varepsilon_{x,0}$ *prior* to compression:

$$LD_\parallel(k;s) = \exp\left\{-\frac{1}{2}[(CkR_{56})_s^2\sigma_{\delta,0}^2]\right\}, \quad (7)$$

$$LD_\perp(k;s) = \exp\left\{-\frac{1}{2}[(C^2k^2H_x)_s\varepsilon_{x,0}]\right\}, \quad (8)$$

and finally

$$H_x = [R_{52}^2 + (\beta_x R_{51} - \alpha_x R_{52})^2]/\beta_x, \quad (9)$$

with standard notation for the horizontal Twiss functions and linear transport matrix terms. In our convention, a four-dipole chicane has positive R_{56}. We note that the assumption of ultrarelativistic electrons commonly allows one to neglect the longitudinal slippage of particles in a nondispersive straight section, which amounts to $z(L) = R_{56}(L)\sigma_\delta < 0.1$ μm for drift length $L \approx 10$ m or so. Hence, the longitudinal charge distribution is "frozen", the bunching factor is frozen as well and, in most cases, $b(k;s')/\gamma(s')$ can be brought out of integration in Eq. (6),

with the meaning of bunching factor evaluated at the beginning of the line and the beam energy at the end of it.

The unity in Eq. (5), before the approximated expression, stays for the nonamplified bunching factor, which states the superposition of initial ("low gain") and amplified modulations ("high gain"). Because of this, the peak gain can, in principle, be made lower than 1 with a suitable choice of the compressor parameters. This is a consequence of the $\pi/2$-phase shift of density and energy modulations, for example, describing shot-noise reduction by virtue of anticorrelated electrons' position [66–68]. Nevertheless, since only density modulations driven by the initial bunching and larger than that are retained in the model, the gain cannot be smaller than 0 (at any wavelength). In realistic cases, the peak gain is always larger than $O(10)$.

In most practical cases, and in the range of wave numbers $k \leq (CR_{56}\sigma_{\delta,0})^{-1}$ at which the bunch can be modulated, one finds $CkR_{56}\frac{\Delta\gamma}{\gamma} < 1$ (i.e., the longitudinal shift of electrons due to longitudinal dispersion is smaller than the compressed modulation wavelength). This allows the linearization $J_1(\zeta) \cong \zeta/2$ in Eq. (5). Higher harmonics of the modulation content are neglected because Landau damping is stronger in proportion to the harmonic number [8]. Since, by virtue of the approximation above, the gain depends at first order on the modulation amplitude, it is said to be in the "linear regime." When $\zeta \geq 1$, $J_1(\zeta)$ can describe a "saturation" effect of the gain due to phase space folding.

We remark that, as long as a symmetric four-dipole chicane is considered, the second order longitudinal dispersion contributes to $LD_{\parallel}$ through $T_{566} = -1.5R_{56}$, but the exponent goes like $\sim T_{566}^2\sigma_{\delta,0}^4$. Hence, in the case of moderate damping ($C^2k^2R_{56}^2\sigma_{\delta,0}^2 \leq 1$), the ratio of $LD_{\parallel}$ at the second and at the first order in the dispersion is approximately $\exp(-C^2k^2R_{56}^2\sigma_{\delta,0}^4) \approx 1 - C^2k^2R_{56}^2\sigma_{\delta,0}^4$, which is close to unity in virtue of the assumption and for $\sigma_{\delta,0} \ll 1$. In conclusion, the damping term at second order in dispersion is approximately 2 orders of magnitude smaller, hence negligible for any practical purpose.

A linear gain approximation implies an independent amplification of each modulation frequency. Second-order corrections in the energy modulation amplitude can be introduced to describe frequency mixing, which may happen for largely distorted phase space, such as at large momentum compaction of the compressors *and* large compression factor. This is described by Eq. (20) in [69], which we recast here for the sake of brevity, by pointing out the gain functional dependence on compressor parameters and peak current:

$$G^2(k;s) = G^1(k;s)[1 + A(kr_b/\gamma)I_0(CkR_{56})^2s^2]. \quad (10)$$

The energy modulation introduced in Eq. (6), induced by a path-length-integrated impedance Z_{int}, can be integrated over all modulation frequencies to provide an equivalent instability-induced slice energy spread (see full derivation in Appendix A):

$$\frac{\sigma_{\gamma,\mathrm{MBI}}^2}{\gamma^2} = \frac{\sigma_z}{2\pi N_e}\int_{-\infty}^{+\infty}\frac{|\Delta\gamma(k)|^2}{\gamma^2}dk = \frac{2ec}{I_0}\int_0^{+\infty}\mathrm{d}\lambda\frac{|\mathrm{G}(2\pi/\lambda)Z_{\mathrm{int}}(2\pi/\lambda)|^2}{\lambda^2}. \quad (11)$$

The total uncorrelated energy spread along the beamline is contributed by the initial uncorrelated energy spread (evaluated at the end of the photoinjector) added in quadrature to the uncorrelated energy spread induced by the laser heater (LH) before any compression, to that one induced by intrabeam scattering (IBS), and to $\sigma_{E,\mathrm{MBI}} = m_ec^2\sigma_{\gamma,\mathrm{MBI}}$. For an approximate preservation of the longitudinal emittance during linear compression, the total uncorrelated energy spread after compression results:

$$\sigma_{E,\mathrm{tot}}^2(s) \cong C^2(\sigma_{E,0}^2 + \sigma_{E,\mathrm{LH}}^2) + \sigma_{E,\mathrm{IBS}}^2(s) + \sigma_{E,\mathrm{MBI}}^2(s) \equiv \sigma_{E,\mathrm{int}}^2(s) + \sigma_{E,\mathrm{MBI}}^2(s). \quad (12)$$

When $\sigma_{E,\mathrm{MBI}}$ is negligible (damped instability), Eq. (12) is expected to provide the actual slice energy spread. This is also approximately the case when $\sigma_{E,\mathrm{MBI}}$ is large, but in the presence of either folded phase space (broken energy-time correlation) or very short modulation wavelengths (the energy-time correlation is preserved at a time scale much shorter than the slice duration). In general, the ratio of Eq. (12) and the value of the uncorrelated energy spread in the absence of instability ("intrinsic", $\sigma_{E,\mathrm{int}}$) can be used as a normalized marker of the instability strength:

$$\frac{\sigma_{E,\mathrm{tot}}}{\sigma_{E,\mathrm{int}}} = \sqrt{1 + \frac{\sigma_{E,\mathrm{MBI}}^2}{\sigma_{E,\mathrm{int}}^2}} \equiv \sqrt{1+\chi^2}, \quad (13)$$

B. Intrabeam scattering

Intrabeam scattering (IBS) is the multiple small-angle Coulomb scattering of charged particles in accelerators, potentially diluting beam transverse and longitudinal emittance. Historically, the emittance growth rate of a beam stored in a synchrotron is calculated either following Piwinski's analytical mechanics [70] or Bjorken and Mtingwa's quantum field theory [71]. The two approaches converge to the same solution in the so-called Bane's high energy approximation [72]. Such an approximation has been adopted to evaluate the increase of uncorrelated energy spread in a drift section at constant energy, and with a residual uncertainty on the so-called Coulomb logarithm (Clog) [73].

Starting from [73], a refined IBS model was proposed in [18] to calculate $\sigma_{E,\mathrm{IBS}}(\gamma;s)$ through accelerating sections and dispersive regions and to eventually compare Eq. (12)

with measurements. The Clog was calculated following the numerical prescription provided originally by Raubenheimer for Gaussian transverse distributions with long tails [74], now adapted to a single-pass beamline with a constant average Lorentz factor $\bar{\gamma}$ ("constant Clog"). The synchrotron radiation damping time is replaced by the traveling time of particles along the linac [18]. When the adiabatic damping of the longitudinal momentum is properly taken into account during acceleration from an initial Lorentz factor γ_0 to a final γ, the IBS-induced relative energy spread is the one in Eq. 7 of [75]:

$$\sigma^2_{\delta,\mathrm{IBS}}(\gamma;s) = \frac{4}{3}\frac{k(\bar{\gamma})}{G_a/(m_e c^2)}\left(\frac{\gamma^{3/2}-\gamma_0^{3/2}}{\gamma^2}\right), \quad (14)$$

where G_a is the average accelerating gradient in MeV/m, $\gamma m_e c^2$ the final electron total energy in MeV, and

$$k(\bar{\gamma}) = a\ln\Lambda = a\ln\left(\frac{\varepsilon_n q_{\max}}{2\sqrt{2}r_e}\right)\Bigg|_{\bar{\gamma}} \cong \left(\frac{N_e r_e^2}{8\varepsilon_n^{\frac{3}{2}}\beta_\perp^{\frac{1}{2}}\sigma_z}\right)\ln\left(\frac{\beta c\tau N_e \varepsilon_n^{\frac{1}{2}}}{16\gamma^{\frac{3}{2}}\beta_\perp^{\frac{1}{2}}\sigma_z}\right)\Bigg|_{\bar{\gamma}}, \quad (15)$$

with $r_e = 2.818\times10^{-15}$ m the classical electron radius, ε_n the transverse normalized emittance, $\beta_\perp$ the average betatron function, N_e the number of electrons in a bunch of rms duration σ_z, and τ the bunch traveling time at speed βc. The approximated value of $q_{\max}$ is still dependent from the beam mean energy, but independent from the uncorrelated energy spread σ_δ at first order in σ_δ.

The explicit dependence of Clog from a varying (s) is taken into account by Eq. (10) in [75], which allows to calculate the IBS-induced energy spread through numerical integration ("integral form"):

$$\sigma^2_{\delta,\mathrm{IBS}}(\gamma;s) = \frac{1}{G_a/(m_e c^2)}\frac{1}{\gamma^2}\int_{\gamma_0}^{\gamma} d\gamma'\sqrt{\gamma'}k(\gamma'). \quad (16)$$

Finally, an approximate closed form of $\sigma_{E,\mathrm{IBS}}(\gamma(s);s)$, with explicit dependence of Clog from the varying beam energy, still at first order in σ_δ, was given in Eq. 29 of [76]. That solution, however, is inaccurate, because it was derived by discarding the momentum damping during acceleration. When this is properly accounted for, we can solve the equation for the energy spread growth rate with the Fourier method (separation of variables), to finally get ("closed-form"):

$$\sigma^2_{\delta,\mathrm{IBS}}(\gamma;s) = \frac{2}{3}\frac{a}{G_a/(m_e c^2)}\frac{1}{\gamma^2}[(1+2\ln\tilde{\Lambda})(\gamma^{3/2}-\gamma_0^{3/2}) + +2(\gamma_0^{3/2}\ln\gamma_0^{3/4} - \gamma^{3/2}\ln\gamma^{3/4})], \quad (17)$$

where $\tilde{\Lambda} = \gamma^{\frac{3}{2}}\Lambda$ and Λ was defined in Eq. (15).

It is intended for Eqs. (14), (16), and (17) that the total uncorrelated relative energy spread in the presence of acceleration is

$$\sigma^2_{\delta,\mathrm{tot}}(\gamma(s);s) = \left(\sigma_{\delta,0}\frac{\gamma_0}{\gamma}\right)^2 + \sigma^2_{\delta,\mathrm{IBS}}(\gamma;s). \quad (18)$$

C. Implementation of the Huang–Kim formalism

The HK formalism relies on the linearization of the Vlasov-Maxwell equation for the 6D electron beam distribution function passing through a four-dipole symmetric chicane [26]. The effect of impedances on the formation of microbunches results in an integral equation with a specific initial condition for the bunching factor, and in which the kernel contains the physics of collective effects, including Landau damping [77]:

$$b(k(s);s) = b_0(k(s);s) + \int_0^s K(s',s)b(k(s');s')ds'. \quad (19)$$

In our implementation, the effect of IBS is evaluated stepwise along the beamline, sketched in Fig. 1 for illustration. The line is split into drift sections (this being either a linac or a transfer line, from s_0 to s_1), interleaved with magnetic chicanes (bunch compressor, from s_1 to s_2 for the first half of the chicane, from s_2 to s_3 for the second half). The initial bunching (defined at s_0) in Eq. (4) generates energy modulation through LSC (up to s_1) according to Eq. (6). That is then plugged into Eq. (5) to calculate the amplified bunching factor in the presence of longitudinal dispersion R_{56} (s_3). The bunching amplification due to the presence of CSR is also calculated following strictly [26], then linearly superimposed to the initial and copropagating bunching (low gain term), and to the LSC-driven bunching (high gain):

$$b(s_3) = b(s_0) + b|_{R_{56}}(s_{0\to3}) + b|_{\mathrm{CSR}}(s_{1\to3}). \quad (20)$$

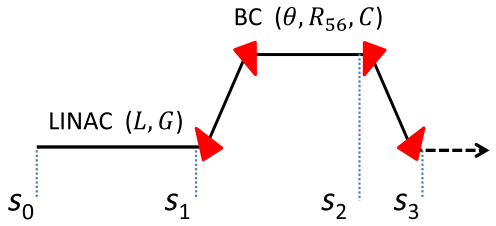

FIG. 1. Sketch of a beamline consisting of a linac section of length L and average accelerating gradient G, followed by a four-dipole magnetic chicane (bunch compressor, BC) characterized by dipole bending angle θ, longitudinal dispersion function R_{56}, and putting in place linear compression by a factor C. This type of beamline can be replicated in a series to model multistage compression. See the text for reference.

Each addendum in Eq. (20)—rhs is solution of Eq. (19) with a specific kernel: the first term is obtained in the absence of collective effects; the second term is calculated through Eq. (5), multiplied by the bunching factor at the beginning of the section under consideration; the third term is calculated according to the solution of the Volterra-type equation provided in [26].

The energy modulation induced by LSC along the chicane (from s_1 to s_3) is also calculated with Eq. (6), where the peak current is assumed to be unperturbed in the first half of the chicane and multiplied by the compression factor in the second half. This energy modulation is superimposed to that one generated in the upstream linac section:

$$\frac{\Delta\gamma}{\gamma}(s_3) = \frac{\Delta\gamma}{\gamma}\bigg|_{0\to1}^{\mathrm{LSC}} + \frac{\Delta\gamma}{\gamma}\bigg|_{1\to2}^{\mathrm{LSC}} + \frac{\Delta\gamma}{\gamma}\bigg|_{2\to3}^{\mathrm{LSC}}. \tag{21}$$

The last two terms of Eq. (21) introduce Landau damping terms similar in form to Eqs. (7) and (8). According to [26], transverse damping is approximated by retaining only the contribution from the fourth dipole of the chicane, traversed by the fully compressed bunch, and where the dispersion $\eta_x \to 0$ so that $H_x \cong \beta_x \eta_x'^2 \cong \beta_x \theta^2$.

Longitudinal damping is driven by the uncorrelated energy spread updated to its value upstream the chicane, namely, $\sigma_{E,\mathrm{int}}$ in Eq. (12). The laser heater is assumed to induce purely uncorrelated energy spread (user-specified) before compression, but the bunching at the exit of the chicane inherits the modification to the idealized Gaussian energy distribution as possibly due to the transverse mismatch of laser (σ_l) and electron beam size (σ_e) in the laser heater undulator, assuming both are round beams. Thus, Eq. (7) becomes [36]:

$$LD_{\|}(k;s_3) = \exp\left[-\frac{1}{2}(CkR_{56})_s^2 \sigma_{\delta,\mathrm{int}}^2(s_1)\right]\xi_0(k;\sigma_e,\sigma_l), \text{and}$$
$$\xi_0 = \int dR R e^{\left(-\frac{R^2}{2}\right)} J_0\left[CkR_{56}\sigma_{\delta,\mathrm{LH}}\exp\left(-\frac{R}{2}\frac{\sigma_e}{\sigma_l}\right)^2\right]. \tag{22}$$

D. Implementation of the Bosch–Kleman-Wu formalism

The BKW theory treats a 2D vector of longitudinal modulations in the current-energy space. All the collective phenomena, namely LSC, CSR, and CER, are introduced by means of impedances $Z_{\mathrm{coll}}(k)$. The contributions to beam modulations are expressed via matrix multiplication, where each matrix is of the general form [27]:

$$T = \begin{pmatrix} b_f/b_i & b_f/\Delta_i \\ \Delta_f/b_i & \Delta_f/\Delta_i \end{pmatrix}, \tag{23}$$

with $\Delta_{\mathrm{i,f}} = \Delta\gamma/\gamma_{\mathrm{i,f}}$ as, e.g., from Eq. (6), and in general, all terms depend on the integrated impedance and the compressor parameters, all specified at a certain k.

As observed in [27], the closed-form formulation for more than two compression stages becomes intractable; an identification of analogous gain and energy modulation terms in HK is immediate only for a single stage compression in the absence of CSR. In our implementation, we define a "collective" matrix for each linac section and split each four-dipole chicane into two halves. The LSC, CSR, and CER impedances are evaluated for each dipole and then linearly summed.

A simple multiplication of the matrices in sequence provides the matrix for the full beamline. This procedure automatically includes low gain terms. The product matrix is eventually applied to the beam's initial 2D vector, $v_0^T(k;s_0) = (b_0(k;s_0),0)^T$. In principle, the instability can also be studied for an arbitrary initial energy modulation. Landau damping terms are inherited by all the 4 matrix terms. In particular, transverse damping is accounted for each individual dipole magnet of the compressor, with $H_{x,o} \cong \beta_{x,o}\theta_o^2$ in outer dipoles of the achromatic insertion and $H_{x,i} \cong L^2\theta_i^2/\beta_{x,i}$ in the inner dipoles.

The simplified longitudinal damping introduced in [27] is generalized to an arbitrary transverse match of laser and electrons in the laser heater and thereby made identical to Eq. (22) for the T_{11} and T_{12} terms (bunching). For the T_{21} and T_{22} terms (energy modulation), the zeroth-order Bessel function of Eq. (22) is replaced by a first-order Bessel function.

III. COMPARISON OF MODELS

A. Longitudinal space charge

HK and BKW are applied to the two linacs in Table I. LSC only is considered at first, and the linear gain is shown in Fig. 2. The largest deviation between the models' prediction is for the 10 GeV linac, characterized by a larger compression factor in the first compressor. In such case, despite a peak gain deviation of ~30%, both models predict $\chi < 0.4$, i.e., no impact of the instability on the energy spread [mainly by virtue of a red shift of the gain, see Eq. (11)]. In general, the models' deviation is not proportional to the gain, which is much larger in the 1.5 GeV two-stage. Table II compares the χ-parameter, which results in substantially the same value in all cases. The deviation in energy modulation and bunching (not shown) reflects the one of gain.

B. Coherent synchrotron and edge radiation

The 1D CSR impedance is now added to the gain calculation. For brevity, only the configuration in which this effect is more evident, i.e., the 10 GeV linac two-stage, is shown in Fig. 3.

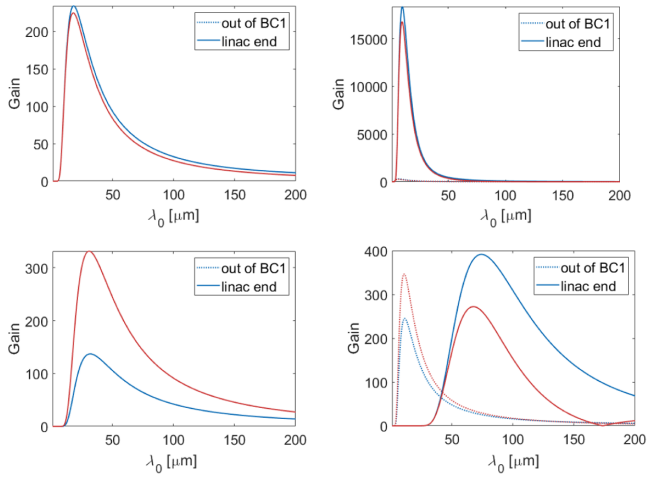

FIG. 2. Gain calculated with HK (blue) and BKW (red), for the 1.5 GeV (top) and 10 GeV linac (bottom), in one- (left) and two-stage compression (right), see also Table I.

Two observations can be drawn. First, HK (left) predicts a larger contribution to the gain from LSC, and a smaller one from CSR, with respect to BKW (right). As a result, the difference in total gain between the two models is 30% right after BC1, but it reduces to ∼5% after BC2. Second, the CSR effect is relevant in BC2 only. This can be attributed to the scaling of the CSR-induced energy modulation amplitude $\delta_{\mathrm{CSR}} \sim (I/E)(R\sigma_z^2)^{-2/3}$, which allows us to estimate $\delta_{\mathrm{CSR}}^{\mathrm{BC2}}/\delta_{\mathrm{CSR}}^{\mathrm{BC1}} \approx 10$ (the $\sigma_z^{-4/3}$ scaling applies exactly to a Gaussian beam and approximately to a flattop one [59]). The BKW calculation is further enriched by the 1D CER impedance. This addition is motivated by the fact that, despite far smaller effect compared to CSR, and thereby not very relevant, our finding is apparently in contrast to the observation in [27], where CER was thought to be the driving force of the instability, though at macroscopic wavelengths $\lambda \approx 2\pi\sigma_z \sim 100$ μm. In fact, Fig. 3 is consistent with those observations, since analogous estimations of the integrated CSR and CER impedance for the case under study here provide $Z_{\mathrm{CER}} \leq 0.5\ \Omega$ and $Z_{\mathrm{CSR}} \approx 2\ \Omega$ per dipole magnet, whereas the opposite situation is reported in [27]. The deviation in total gain driven by LSC and CSR for all other cases considered in Fig. 2, as well as in energy modulation and χ-parameter, is smaller than 5% (not shown). We remark that the inclusion of CER in the HK model would require a major modification to the kernel of the integral linearized Vlasov-Maxwell equation, and it therefore deserves a dedicated effort.

TABLE II. χ-parameter [Eq. (13)] calculated for the configurations in Fig. 1. LSC is the only collective effect included.

	1.5 GeV		10 GeV	
	χ^{HK}	χ^{BKW}	χ^{HK}	χ^{BKM}
One-stage	2.9	3.0	0.1	0.1
Two-stage	99	107	0.3	0.4

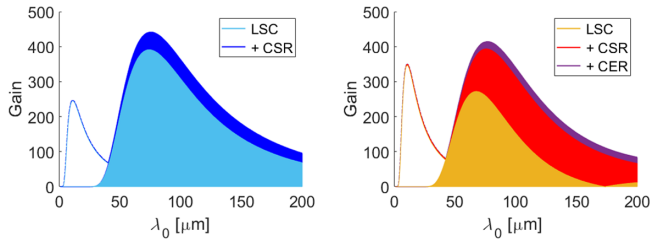

FIG. 3. Gain of the 10 GeV linac after BC1 (dashed, peak at shorter wavelengths) and after BC2 (solid), according to HK (left) and BKW (right). The gain driven by LSC-only is increased by CSR after BC2 and further increased by CER in the BKW.

C. Intrabeam scattering

Since the IBS-induced damping of the instability is more effective for larger product CR_{56} [see Eq. (7)], we expect its effect to be more visible when such product, and hence the gain, is larger; this is the case of the 1.5 GeV two-stage set (see Fig. 2). The effect of the three IBS models in Eqs. (14), (16), and (17) is compared in each formalism, and the total gain is shown in Fig. 4. Table III compares the χ parameter.

Regardless of the compression scheme, and for each IBS model, HK and BKW continue to agree well (within 10% in gain). The gain reduction induced by IBS (with respect to Fig. 2, where IBS was not included) is only a factor of ∼1.3 for the one-stage and ∼4 for the two-stage.

Both in HK and in BKW, the deviation in gain and energy spread for the three IBS models results proportional to the gain. In particular, the models provide substantially the same final energy spread for the one-stage, while a peak-to-peak deviation of approximately 45% is found for

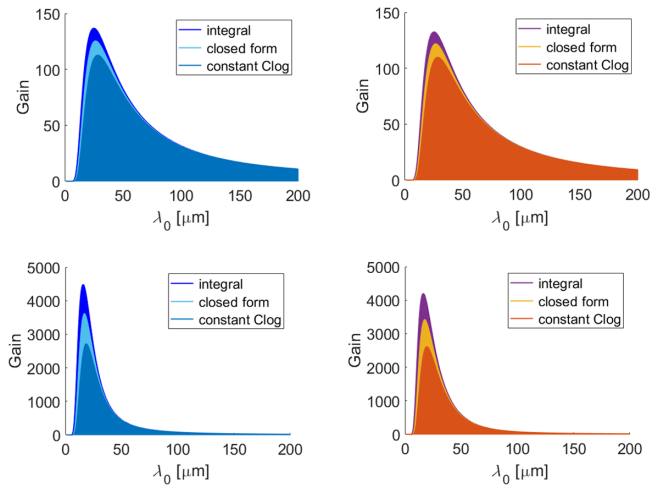

FIG. 4. Total gain of the 1.5 GeV one-stage (top) and two-stage set (bottom), from HK (left) BKW (right). Collective effects include LSC and CSR. IBS is modeled according to Eqs. 14 (constant Clog), (16) (integral form), and (17) (closed form).

TABLE III. χ-parameter [Eq. (13)] and final slice energy spread [Eq. (12)] calculated for the 1.5 GeV linac in one- and two-stage compression, in HK and BKW, and with IBS according to Eqs. (14), (16), and (17); see also Fig. 4.

IBS model	χ^{HK}	σ_E^{HK} (keV)	χ^{BKW}	σ_E^{BKW} (keV)
		One-stage		
Integral form [Eq. (16)]	2	53	2	52
Closed form [Eq. (17)]	2	53	2	52
Constant Clog [Eq. (14)]	2	55	2	54
		Two-stage		
Integral form [Eq. (16)]	18	421	19	446
Closed form [Eq. (17)]	13	320	14	345
Constant Clog [Eq. (14)]	9	223	10	248

the two-stage. The IBS effect is gradually overestimated, passing from the integral form [(Eq. (16)] to the closed form [Eq. (17)], to the constant Clog [Eq. (14)]. This is not totally unexpected. A closer inspection of Eqs. (14), (16), and (17) for the simplified scenario in which $k(\gamma) \cong$ const and $\gamma \gg \gamma_0$, shows that the IBS-induced energy spread goes like $\sigma^2_{\delta,\mathrm{IBS}}(\gamma \to \infty) \propto \frac{g}{\sqrt{\gamma}}$, with g a numerical coefficient equal to $4/3$ for the constant Clog, $2/3$ for the closed form, and $< 2/3$ for the integral form. In the remaining of this article, the integral form for IBS is used, unless differently specified.

D. Laser heater

The modification to the gain by beam heating is studied in Fig. 5 for three heating levels (weak, moderate, and large), and for the electron and laser beam transversally matched, and mismatched by a factor $B_{\mathrm{LH}} = \sigma_l/\sigma_e = 1.5$. We keep considering the 1.5 GeV linac two-stage compression, as it still shows the largest gain in the presence of LSC, CSR, and IBS (see Fig. 4).

Figure 5 confirms the good agreement of HK and BKW for any laser heater setting. A mismatched laser pulse generates a richer spectral distribution of the gain at short wavelengths when $\sigma_{E,\mathrm{LH}} \gg \sigma_{E,0}$, consistently with the trend observed in [78]. It is also slightly more effective (lower peak gain) than for a perfectly matched beam when $\sigma_{E,\mathrm{LH}} \approx \sigma_{E,0}$, as also experimented in [79].

According to Eqs. (11) and (12), the agreement in the prediction of the gain has to reflect in the final slice energy spread or, equivalently, in the χ-parameter, as indeed shown in Fig. 6-top plot. Figure 6-bottom shows the "optimum" laser heater setting, i.e., the energy spread induced by the heater in

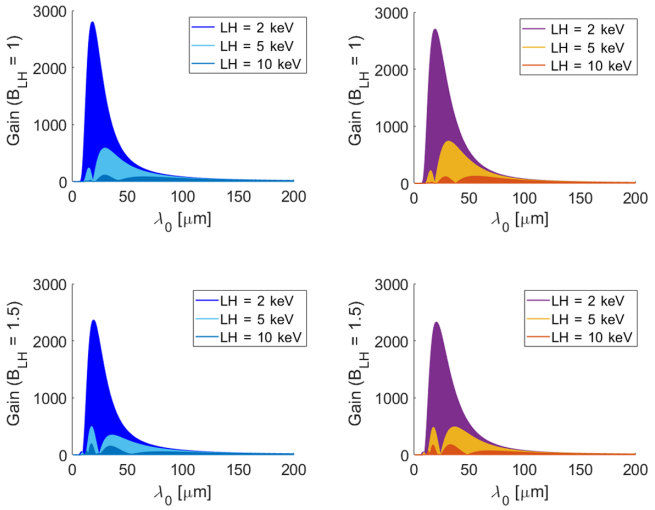

FIG. 5. Total gain of the 1.5 GeV two-stage set, from HK (left) and BKW (right), in the presence of LSC, CSR, IBS [Eq. (16)], and laser heater. The laser transverse size is matched (top) and mismatched (bottom) to the electrons.

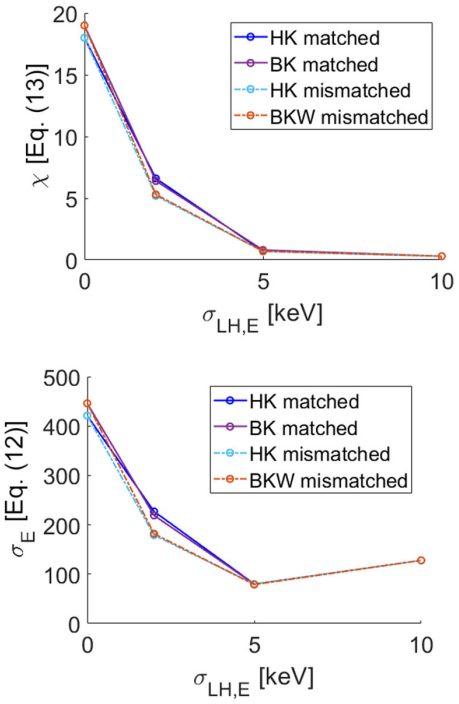

FIG. 6. χ-parameter (top) and final slice energy spread (bottom) corresponding to Fig. 5, as a function of the uncorrelated energy spread induced by the laser heater, for HK (blue) BKW (red), matched (solid), and mismatched beams (dashed).

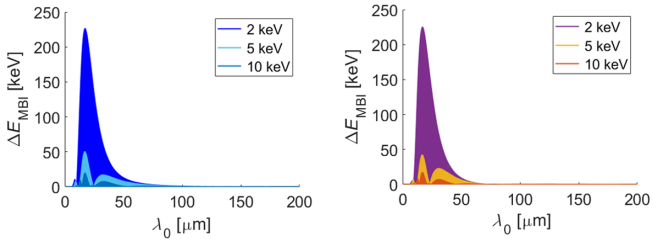

FIG. 7. Energy modulation amplitude corresponding to the gain in Fig. 5-bottom row, from HK (left) and BKW (right).

correspondence of which the final slice one is minimized, though the instability is not fully damped ($\chi \approx 1$).

For completeness, Fig. 7 shows the excellent agreement of HK and BKW also in the prediction of the spectrum of the energy modulation, for the same configuration of Fig. 5. Not shown for brevity, the same agreement is found for all cases considered so far, when all collective effects are included. We note that the largest deviation in gain and final energy spread between the matched and mismatched LH is, as expected, for moderate heating levels, i.e., when the LH is active but the instability is still strong. This corresponds to the setting $\sigma_{E,\mathrm{LH}} = 2$ keV in Figs. 5 and 6. In such case, the peak gain is reduced from approximately 2800 to 2350, χ varies from 6.5 to 5, and the final energy spread from 235 to 190 keV.

E. Linear and nonlinear gain corrections

Having assessed the good agreement of HK and BKW in a wide range of parameters and configurations once all major collective effects are included, the impact of low gain terms [Eq. (5)] and second-order correction to the gain [Eq. (10)] is evaluated below with HK only, since it is particularly well suited to switch each individual contribution on and off in the calculation. Figures 8 and 9 show the final gain for the 1.5 and 10 GeV linac, respectively, with and without beam heating. All four cases in Fig. 2, now including the full set of features, i.e., LSC, CSR, and IBS, are illustrated.

It turns out that low gain terms can be neglected when the peak gain is $\sim O(10)$ or larger (see Fig. 8). For any given (small) gain, low gain terms are more relevant at longer wavelengths and, for the two-stage compression, still proportional to the product CR_{56} in BC1 (compare Figs. 8 and 9). By virtue of their relevance at small gain and long wavelengths, low gain terms tend not to contribute to the final slice energy spread directly, although they can modify further developments of the instability (see more later).

The second-order correction to the gain does not change the picture substantially even. When the linear gain is high, the final slice energy spread is increased by the second order by 10% or so. When the linear gain is low, and in proportion to the product CR_{56}, the second-order correction

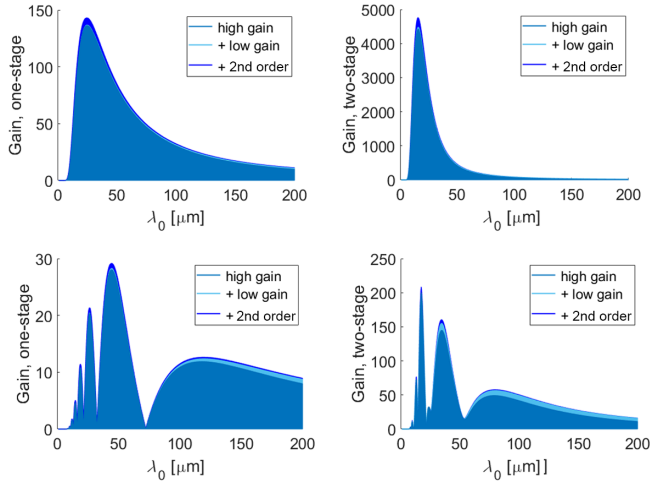

FIG. 8. Total gain for the 1.5 GeV linac, without (top) and with beam heating of 10 keV rms (bottom), for one- (left) and two-stage compression (right). LSC, CSR, and IBS are all included. Low gain terms and second-order correction are incrementally added. The low gain contribution (lightest blue) is basically null without beam heating (top). The second-order correction (dark blue) is barely visible with beam heating (bottom).

can further amplify the linear gain by a factor of ∼5–10. Nevertheless, the energy spread remains substantially unaffected owing to the fact that the instability is damped in this case.

The second-order correction dominates the gain, and therefore, becomes essential to the final energy spread, in a scenario where a large CR_{56} product and a high linear gain coexist (see also [69]). This, however, is not a realistic picture since it can only be obtained in the absence of IBS, as shown in Fig. 10.

A final check of the self-consistency of the implementation of HK and BKW is carried out by looking to the

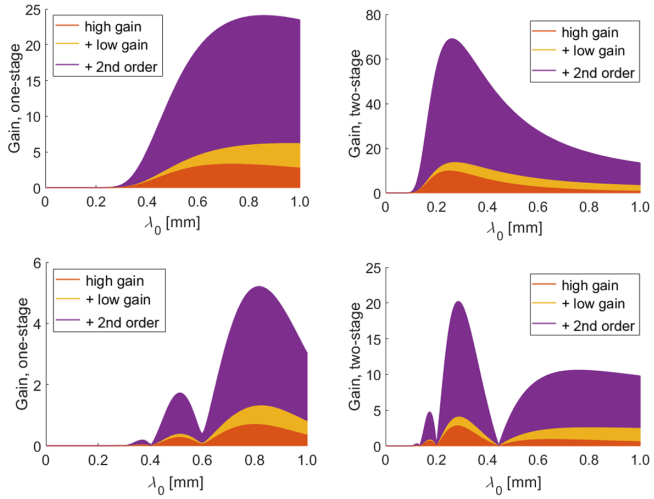

FIG. 9. Same as in Fig. 8, here for the 10 GeV linac and 5 keV rms heating level (bottom).

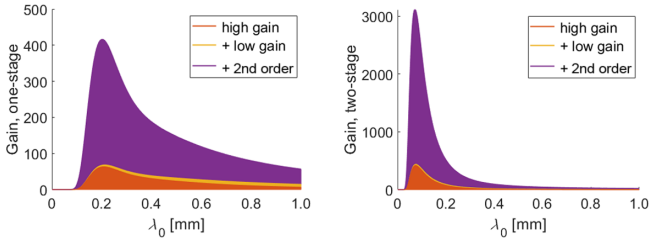

FIG. 10. Same as in Fig. 9, with neither heating nor IBS. The final slice energy spread is almost doubled by the second-order correction in the two-stage compression. In both plots, the low gain contribution (yellow) is barely visible.

dependence of the final gain from the initial bunching, the initial peak current, and to the validity of linearization of the Bessel function in the expression of the gain of Eq. (5).

According to Eq. (5), G^1 is independent from b_0, and hence, the final bunching is linearly proportional to that. The same behavior is expected for G^2, which, for any fixed initial current I_0, inherits the same dependence of G^1 from b_0 [see Eq. (10)]. Indeed, this is confirmed in Fig. 11 (only the set with largest gain in Fig. 2, i.e., 1.5 GeV two-stage, is illustrated for brevity).

While expected, this result is in contrast with the conclusion in [80], where a nonlinear theory of MBI predicts a dependence of the gain from b_0. The discrepancy can be attributed to the fact that the authors, while still modeling the instability as a linear superposition of Fourier components, do not linearize the gain [Bessel function in Eq. (5)], which can therefore imply a less obvious residual dependence of G^1 from b_0. At the same time, one could argue that any deviation from monochromaticity makes the use of the Bessel function, which implies a linear superposition of purely sinusoidal monochromatic modulations, inconsistent, as shown in [69]. The license to linearization in our implementation of HK and BKW is discussed below.

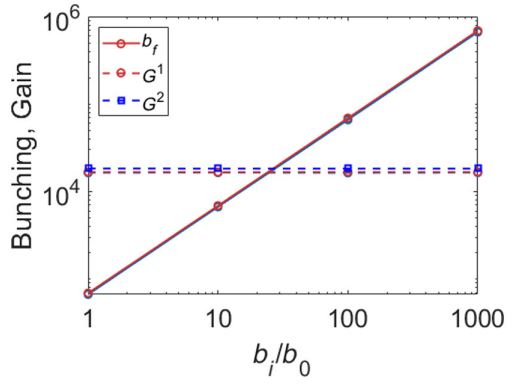

FIG. 11. Peak value of the final bunching (solid) and gain (dashed) for the 1.5 GeV two-stage set vs initial bunching factor normalized to shot noise level. LSC and CSR only included. Result from HK (blue) and BKW (red) superimpose.

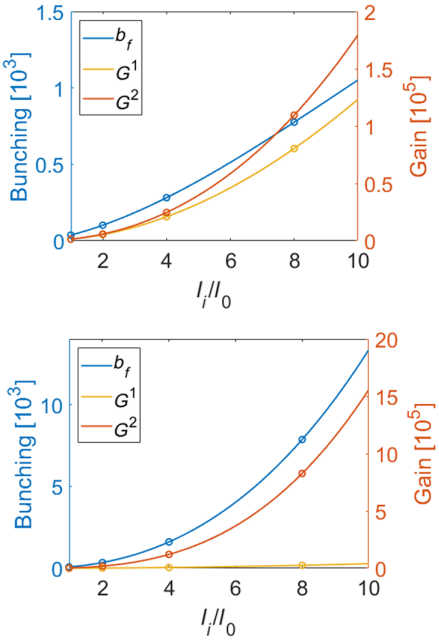

FIG. 12. Peak value of the final bunching (blue), linear (yellow), and nonlinear gain (orange), for the 1.5 GeV (top) and 10 GeV two-stage set (bottom), as a function of the normalized initial peak current. LSC and CSR only included.

The dependence of the gain from the initial peak current is even less immediate since the evolution of the bunching through multiple energy-to-density conversion stages can make $b_f \propto I_0^\alpha$, with $\alpha \geq 1$. This is investigated in Fig. 12 with HK for the linear and nonlinear gain (the 1.5 and the 10 GeV two-stage sets, without IBS to maximize the gain, are considered).

A fit to the numerical data of the 1.5 GeV (10 GeV) linac provides $\alpha \cong 1.5$ (2.2) for the bunching, 2 (2.1) for the linear gain, and 2.1 (2.9) for the nonlinear gain. This is consistent with the observation, drafted from Figs. 8 to 10, that the 1.5 GeV linac is insensitive to the second-order correction, while the 10 GeV linac largely is. In such case, the numerical results also agree well with the prediction of Eq. (10), according to which, if $G^1 \propto I_0^\alpha$, then $G^2 \propto I_0^{\alpha+1}$.

Finally, the validity of the linearization of the Bessel function in Eq. (5) is justified *a posteriori* in Fig. 13, where the argument $\zeta(\tilde{\lambda})$ is calculated at the entrance of the compressors, for the wavelength at which the gain is maximum, $\tilde{\lambda} = 2\pi C R_{56} \sigma_{\delta,\mathrm{i}}$, and $\sigma_{\delta,\mathrm{i}}$ is the relative uncorrelated energy spread at the entrance of the compressor. In such case, one simply has $\zeta(\tilde{\lambda}) = \zeta_c = \Delta E(\tilde{\lambda})/\sigma_{E,0}$. The calculation is conducted for all four cases in Fig. 1, now including LSC, CSR, and IBS. The calculation is possibly overestimating ζ, not only because beam heating is not included (which would make ζ_c much smaller) but also because the argument is much smaller at wavelengths slightly longer than $\tilde{\lambda}$, where the gain is still high (see Figs. 8 and 9, top row).

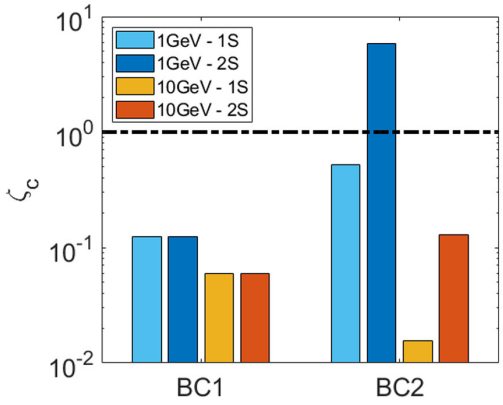

FIG. 13. Argument of the gain Bessel function in Eq. (5), calculated at the entrance of bunch compressors, in correspondence of the wavelength of maximum gain, for all four cases in Fig. 2, and with LSC, CSR, and IBS included. The linearization of the Bessel function in Eq. (5) is a good approximation for $\zeta_c < 1$.

We conclude that the linearization of the Bessel function is overall justified, with the exception of the 1.5 GeV, two-stage set. In this case, owing to the relatively large energy modulation at the entrance of BC2, the final gain could be overestimated by the linearization. In addition, one could reasonably argue that the inclusion of second-order correction to the gain [Eq. (10)] in the presence of gain linearization [Eq. (5)], whenever the latter is admitted by virtue of small electrons' phase slippage, is not a fully self-consistent procedure. In such a case, the gain at second order tends to illustrate a pessimistic scenario.

IV. BENCHMARK OF MEASUREMENTS

A. FERMI high charge

The HK formalism was first and successfully applied in [18] to explain the observed ~100 keV slice energy spread at the end of the FERMI linac in a low charge regime (100 pC), for which IBS was shown to play a critical role in limiting the MBI gain. The exercise is repeated here for the slice energy spread measured at the same facility in high charge regime (600 pC) and reported in Fig. 2 of [81].

Figure 14 compares $\sigma_{E,\mathrm{tot}}$ predicted by HK and BKW to the slice energy spread $\sigma_{E,m}$ measured at the entrance of the FERMI FEL undulator line, at the energy of 1.32 GeV, for the three peak currents of 0.8, 1.1, and 1.3 kA. The comparison is carried out for no heating and for heating inducing 5 keV rms energy spread (approximately 1 μJ laser pulse energy). The modeling includes the 25-m-long FERMI high energy transfer line connecting the linac to the undulator: it is treated as a straight section, neglecting its small $|R_{56}| <$ 1 mm and hence CSR in the four dipoles, while LSC and IBS are included. Doing so, the present modeling is missing the

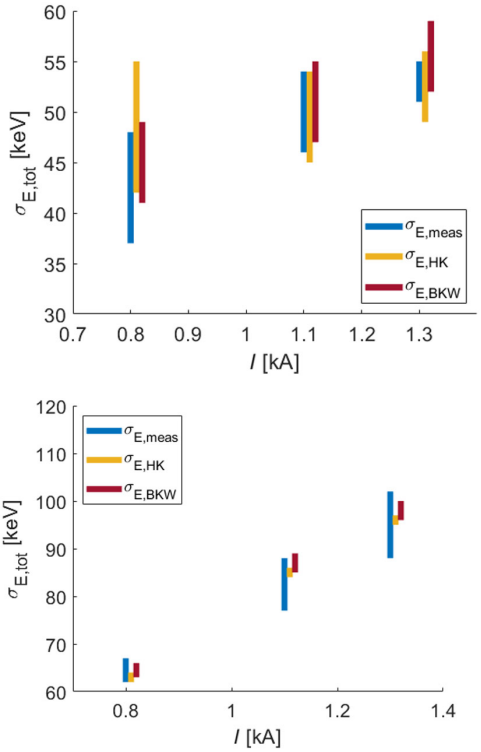

FIG. 14. Slice energy spread at the entrance of the FERMI undulator line predicted by HK (orange), BKW (red), and measured [81] (blue), for laser heater off (top) and inducing 5 keV rms energy spread (bottom). See text for the meaning of bars.

potential impact of phase mixing, energy or emittance damping developing through the transfer line [13,17,82,83].

The initial peak current is estimated to be ~600 pC/8 ps = 75A, and thereby the compression factor in BC1 results in $C \cong 11(0.8\ \mathrm{kA})$, 15 (1.1 kA), and 17 (1.3 kA). Assuming that $\sigma_{E,m}$ with no heating is weakly affected by the instability, the uncorrelated energy spread at the entrance of BC1, at a beam energy of 300 MeV, is estimated as the minimum among the values $\sigma_{E,\mathrm{BC1}} = \min(\sigma_{E,m}/C) = \min(3.0, 3.3, 3.7) = 3.0$ keV, where $\sigma_{E,m} =$ 41, 50, 53 keV respectively. To retrieve the uncorrelated energy spread at the exit of the photoinjector, ~20 m upstream BC1 and at the beam energy of 100 MeV, we subtract in quadrature from $\sigma_{E,\mathrm{BC1}}$ the minimum energy spread induced by IBS along that region, i.e., 1.8 keV, and eventually fix the initial energy spread to $\sigma_{E,0} = 2.4$ keV.

Figure 14 confirms the mutual agreement of HK and BKW and of their prediction with measurements [81], with and without beam heating. The height of the vertical blue bars corresponds to the experimental uncertainty reported in [81]. The height of the orange and red bars corresponds to the peak-to-peak variation of the prediction over all three IBS models in Eqs. (14), (16), and (17), and for average betatron functions along the FERMI beamline scanned in

the range of 10–20 m. It is worth stressing that the models do not imply any fitting procedure.

We observe that the prediction becomes more and more insensitive to IBS and beam optics when the instability is largely damped by the laser heater (shorter orange and red bars in the bottom plot). Unlike for the low charge regime reported in [18], the final energy spread is here basically the same with and without IBS, apart from a redistribution of the intrinsic and MBI-induced energy spread along the line. This is confirmed independently from the IBS model adopted. The maximum deviation in the final energy spread, for any given linac configuration, is less than 2 keV. CSR, low gain terms, and nonlinear gain all contribute to the increase of the final energy spread by less than 3% (not shown).

B. LCLS low charge

In some cases, the inclusion of IBS is crucial to a reliable prediction of the MBI gain and thereby of the final slice energy spread, as suggested, e.g., by comparing Fig. 2 with Figs. 4 and 5, and already reported in [18]. This is also shown to be the case in Fig. 15, where the prediction from HK theory, with IBS [solid line and orange lower triangles for Eqs. (16) and (17); orange square dot for Eq. (14)] and without IBS (dashed line, orange circle), is compared to LCLS experimental data reported in [39]. A 180-pC bunch charge is compressed in two-stage to 1 kA ($C \cong 35$). The final energy is 4.3 GeV, and the initial uncorrelated energy spread is $\sigma_{E,0} = 1$ keV.

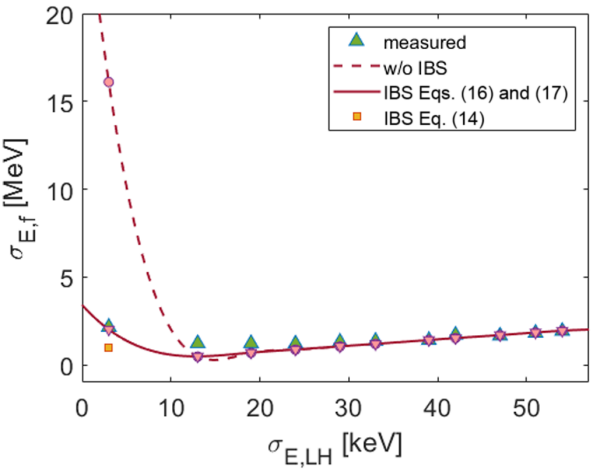

FIG. 15. Final slice energy spread as function of laser-induced energy spread at the LCLS. Experimental data (upper green triangles) are from [39]. Orange symbols are from HK, in correspondence of the experimental data, and they superimpose for $\sigma_{E,LH} > 10$ keV (only lower triangles shown for illustration). In particular, solid line and lower triangles are for IBS as in Eqs. (16) and (17); the two IBS models provide the same final energy spread to any meaningful numerical accuracy. Dashed line and circles are from HK without IBS. Squares are from HK with IBS as in Eq. (14).

For $\sigma_{E,LH} > 10$ keV, the instability is largely damped, $\sigma_{E,IBS}, \sigma_{E,MBI} \ll C\sigma_{E,LH}$, and therefore one finds $\sigma_{E,f} \cong C\sigma_{E,LH}$. At low beam heating, instead, the measured data can only be recovered by including Landau damping from IBS (compare dashed and solid line; the deviation in the absence of IBS is not due to the approximation of linear gain, as initially supposed in [39]).

It is worth pointing out that HK and BKW predict $\sigma_{E,f}$ also in this case with a deviation smaller than 5% in the absence of heating and < 1% with heating. Both in HK and BKW (but only HK shown), the IBS modeled with Eqs. (16) and (17) provide the same result, while Eq. (14) overestimates the IBS-induced energy spread, therefore predicting a stronger damping of the instability and $\sigma_{E,f}$ twofold smaller at low heating (orange square dot).

C. SwissFEL low charge

The proposed modeling of MBI is further tested against experimental data of slice energy spread collected at the SwissFEL for an uncompressed 200 pC charge bunch, see Fig. 16. The experiment is reported in [40], as a function of the laser heater chicane R_{56}, for the downstream BC1 chicane turned off and on, but still $C = 1$. The theoretical benchmark of measurements proposed in [40] adopts the IBS model in Eq. (14), but with the Clog scaled by a fitting coefficient $\alpha = 2.4$. It is shown below that the models proposed in Eqs. (14)–(17) provide similarly good agreement with the observations, without the need for any fitting.

Since the proposed IBS theory is derived for ultra-relativistic beams, the SwissFEL beamline is modeled here as an initial short drift section at 150 MeV, followed by the laser heater chicane, then a linac accelerating to 300 MeV

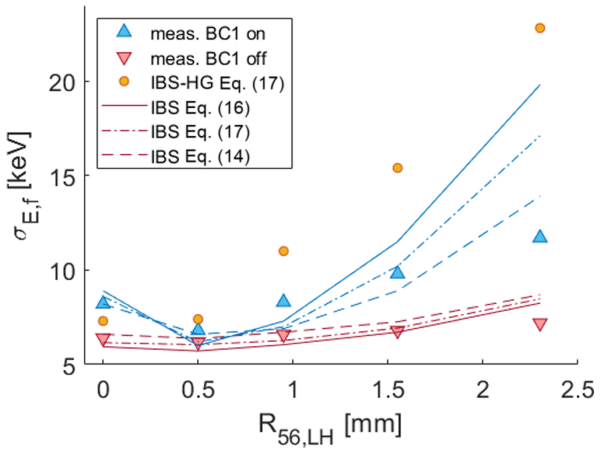

FIG. 16. Final slice energy spread as function of $R_{56,LH}$ at the SwissFEL. Experimental data with BC1 chicane turned on (upper blue triangles) and off (lower red triangles) are taken from Fig. 6 in [40]. Theoretical data, including IBS, are from HK with (blue lines for BC1 turned on and red lines for BC1 turned off) and without low gain terms (orange circles, BC1 turned on).

up to BC1, and eventually the diagnostic line. To take into account the possible impact of IBS from the gun to the laser heater area, and following [40], an initial energy spread of 4 keV at 150 MeV is assumed. The change in beam optics downstream of BC1 when the chicane is turned off is implemented as an effective 30% average larger beam size.

The predictions in Fig. 16 (lines) well reflect the observed minimum of slice energy spread for $R_{56,\mathrm{LH}} = 0.5$ mm (upper triangles). The analysis reveals that the minimum (also barely noticeable for BC1 tuned off, lower triangles) shows up by virtue of the cancellation of low and high gain terms in Eq. (5), in correspondence with which the peak gain lowers to 60 at the wavelength of 8 μm (not shown). To demonstrate this, the energy spread predicted by using Eq. (17) without low gain terms and BC1 turned on is also shown with orange circles (to be compared with upper triangles and dash-dotted blue line).

V. OBLIQUELY INCIDENT LASER HEATER

A. Motivation and background

The aforementioned analysis suggests investigating linac-FEL configurations in which the laser heater chicane is removed so as to avoid any additional energy-to-density conversion stage turning into a deleterious and uncontrolled growth of energy spread at the FEL undulator. Strictly speaking, the electron-laser interaction in the laser heater undulator does not require *per sé* a chicane, and the laser-induced energy modulation, in the range of ∼0.5–1 μm, can be translated into uncorrelated energy spread by smearing through the downstream BC1. To the best of our knowledge, the FLASH laser heater system is the only one implementing such a scheme [84,85]. However, a minichicane is still present upstream of the undulator to inject the laser collinear to the electrons.

In the following, we evaluate the increase in laser peak power required by any predetermined induced energy spread in the presence of an oblique superposition (e.g., in the horizontal plane) of laser and electrons. It is evident that the proposed scheme can, on the one hand, save several meters of space that would otherwise be occupied by the laser heater chicane. Moreover, it can offer a more efficient laser-electron interaction, thus a reduced laser power per induced energy spread, by virtue of smaller electron and laser beam spot size, owing to the absence of dispersive electron motion. On the other hand, the increase of peak power due to the larger effective interaction area has to remain compatible with the available average laser power, such as at superconducting linac-FELs requiring beam heating up to MHz repetition rate.

The energy modulation amplitude of an electron bunch induced by an external laser at an angle of interaction θ was derived in [86]. Equations (21)–(23) describing the induced energy modulation amplitude in that paper are recast here for the reader's convenience:

$$\begin{aligned}\Delta\gamma_{\mathrm{LH}}(\theta) &= \left(\frac{eE_0N_u\lambda_u}{m_ec^2}\right)\sqrt{I_x(L_u)I_y(L_u)} \\ &\quad\cdot \sin[-\varsigma + a\sin(2\varsigma) + d\cos(\varsigma)] \\ &\quad\cdot [o + p\sin(\varsigma) + q\cos(2\varsigma)]_\varsigma \\ &\equiv \left(\frac{eE_0N_u\lambda_u}{m_ec^2}\right)\Sigma_{JJ}(\theta). \end{aligned} \tag{24}$$

The following quantities have been introduced:

$$\begin{aligned}\varsigma &= k_u z \\ a &= \frac{K^2}{4+2K^2+4\gamma^2\theta^2} \\ d &= \frac{k_s K\sin\theta}{k_u\gamma} \\ o &= \left[\frac{1}{2\gamma^2}\left(1+\frac{K^2}{2}\right)-1\right]\sin\theta \\ p &= -\frac{K\cos\theta}{\gamma} \\ q &= -\frac{K^2}{4\gamma^2}\sin\theta \\ I_{x,y}(L_u) &= \frac{1}{L_u}\int_{-L_u/2}^{L_u/2} dz\,\frac{\sigma_L}{\sqrt{\sigma^2_{e(x,y)}(z)+\sigma_L^2(z)}}, \end{aligned} \tag{25}$$

where E_0 is the laser peak electric field, $L_u = N_u\lambda_u$ the number of undulator periods times the period length, z is the longitudinal coordinate internal to the bunch, $k_u = 2\pi/\lambda_u$, $k_s = 2\pi/\lambda_s$ the laser wave number, and K the undulator parameter planarly polarized. The correction factors $I_{x,y} \le 1$ were introduced following [87] to describe the hourglass effect of laser and electron beam at a waist in the middle of the undulator.

The peak power P_L and the peak intensity I_L of a Gaussian laser pulse, whose transverse size at the waist is $w_0 = 2\sigma_L$, are

$$P_L = \frac{1}{2}I_L\pi w_0^2 = \pi c\varepsilon_0 E_o^2\sigma_L^2. \tag{26}$$

With the definition of $P_0 = \frac{4\pi c\varepsilon_0}{e^2}(m_ec^2)^2 = 8.7$ GW and from Eq. (24), the rms-induced energy spread becomes

$$\sigma_{E,\mathrm{LH}}(\theta) = m_ec^2\frac{\Delta\gamma_{\mathrm{LH}}(\theta)}{\sqrt{2}} = m_ec^2\frac{\sqrt{2}L_u}{\sigma_L}\sqrt{\frac{P_L}{P_0}}\sqrt{I_xI_y}\Sigma_{JJ}(\theta). \tag{27}$$

The evaluation of $\Sigma_{JJ}(\theta)$ through numerical integration implies some relevant computation effort in case of optimization studies, for which the overall MBI gain of the beamline is to be minimized as a function of the beam,

machine parameters, and laser heater setting. For this reason, we provide below, as an alternative, a series representation. The mathematical passages outlined below are complemented by ancillary demonstrations in Appendix B.

B. Series representation of induced energy spread

Let us introduce the following notation for the trigonometric terms in Eq. (24):

$$\begin{aligned} o\langle\ldots\rangle_o &= o\cdot\langle\sin[-\varsigma + a\sin(2\varsigma) + d\cos(\varsigma)]\rangle_\varsigma \\ p\langle\ldots\rangle_p &= p\cdot\langle\sin[-\varsigma + a\sin(2\varsigma) + d\cos(\varsigma)]\sin(\varsigma)\rangle_\varsigma \\ q\langle\ldots\rangle_q &= q\cdot\langle\sin[-\varsigma + a\sin(2\varsigma) + d\cos(\varsigma)]\cos(2\varsigma)\rangle_\varsigma \end{aligned} \tag{28}$$

and o, p, q are taken out from the integration (averaging) because independent from ς. Equation (28) is rewritten with Euler notation; $p\langle\ldots\rangle_p$ is taken hereafter as an example:

$$\begin{aligned} \langle\ldots\rangle_p &= -\frac{1}{4}\langle e^{ia\sin(2\varsigma)}e^{id\cos(\varsigma)} - e^{-2i\varsigma}e^{ia\sin(2\varsigma)}e^{id\cos(\varsigma)} + cc\rangle_\varsigma \\ &\equiv \frac{1}{4}[(\langle l\rangle - \langle t\rangle) + (\langle l^*\rangle - \langle t^*\rangle)]. \end{aligned} \tag{29}$$

It can be shown that $\langle l\rangle = \langle l^*\rangle$ and $\langle t\rangle = \langle t^*\rangle$ so that Eq. (29) simplifies to

$$\begin{aligned} \langle\ldots\rangle_p &= -\frac{1}{2}(\langle l\rangle - \langle t\rangle) \\ &= -\frac{1}{4\pi}\left(\int_0^{2\pi} d\varsigma e^{ia\sin(2\varsigma)}e^{id\cos(\varsigma)} + \right. \\ &\quad \left. - \int_0^{2\pi} d\varsigma e^{-2i\varsigma}e^{ia\sin(2\varsigma)}e^{id\cos(\varsigma)}\right). \end{aligned} \tag{30}$$

The integrals in Eq. (30) can be calculated by means of the Jacobi-Anger expansion in Euler form:

$$\begin{aligned} e^{\pm iz\sin(\varsigma)} &= \sum_{n=-\infty}^{\infty} J_n(z)e^{\pm in\varsigma}, \\ e^{\pm iz\cos(\varsigma)} &= \sum_{n=-\infty}^{\infty} (\pm i)^n J_n(z)e^{in\varsigma}, \end{aligned} \tag{31}$$

where J_n are Bessel function of first kind and order n. Hence, the first integral in Eq. (30) results in

$$\begin{aligned} \langle l\rangle &= \frac{1}{2\pi}\int_0^{2\pi} d\varsigma e^{ia\sin(2\varsigma)}e^{id\cos(\varsigma)} \\ &= \frac{1}{2\pi}\int_0^{2\pi} d\varsigma\left[\sum_{n=-\infty}^{\infty} J_n(a)e^{2in\varsigma}\right]\left[\sum_{m=-\infty}^{\infty}(i)^m J_m(d)e^{im\varsigma}\right] \\ &= \frac{1}{2\pi}\sum_{n=-\infty}^{\infty} J_n(a)\sum_{m=-\infty}^{\infty}(i)^m J_m(d)\int_0^{2\pi} d\varsigma\, e^{i\varsigma(2n+m)}. \end{aligned} \tag{32}$$

The following equality is now considered:

$$\int_{-\pi}^{\pi} d\varsigma c_n e^{i\varsigma(m+k)} = 2\pi c_n \delta_{(m+k),0}. \tag{33}$$

This allows us to rewrite the integral in $d\varsigma$ of Eq. (32):

$$\langle l\rangle = \sum_{n=-\infty}^{\infty}\sum_{m=-\infty}^{\infty}(i)^m J_m(d)J_n(a)\delta_{(2n+m),0} \tag{34}$$

which, for the condition $m = -2n$, reduces to

$$\langle l\rangle = \sum_{n=-\infty}^{\infty}(i)^{-2n}J_n(a)J_{-2n}(d). \tag{35}$$

By recalling the Bessel functions' property $J_{-n}(z) = (-1)^n J_n(z)$, and by taking $(i)^{-2n} = (-1)^{-n}$, we are able to recast Eq. (35) in a different notation:

$$\langle l\rangle = \sum_{n=-\infty}^{\infty} J_{-n}(a)J_{-2n}(d). \tag{36}$$

Moreover, by definition of the multivariable generalized Bessel function:

$$J_n^{p,q}(x,y) = \sum_{k=-\infty}^{\infty} J_{M-qk}(x)J_{N+pk}(y), \tag{37}$$

where $n = pM + qN$, Eq. (36) can be further manipulated and rewritten as

$$\langle l\rangle = J_0^{-2,1}(a,d). \tag{38}$$

With the same procedure conducted above, one computes

$$\langle t\rangle = \frac{1}{2\pi}\sum_{n=-\infty}^{\infty} J_n(a)\sum_{m=-\infty}^{\infty}(i)^m J_m(d)\int_0^{2\pi} d\varsigma\, e^{i\varsigma(2n+m-2)}$$
$$= \sum_{n=-\infty}^{\infty}\sum_{m=-\infty}^{\infty}(i)^m J_m(d)J_n(a)\delta_{(2n+m-2),0}$$
$$= \sum_{n=-\infty}^{\infty}(i)^{2-2n}J_n(a)J_{2-2n}(d)$$
$$= -\sum_{n=-\infty}^{\infty}J_{-n}(a)J_{2-2n}(d) = -J_2^{-2,1}(a,d). \quad (39)$$

Equations (38) and (39) provide the final form of Eq. (29) in terms of Bessel functions only:

$$\langle\ldots\rangle_p = -\frac{1}{2}[\langle l\rangle - \langle t\rangle]$$
$$= -\frac{1}{2}[J_0^{-2,1}(a,d) + J_2^{-2,1}(a,d)]\frac{n!}{r!(n-r)!}. \quad (40)$$

It is worth pointing out that by virtue of the property of Bessel functions $J_n(0) = 1$ for $n = 0$ and $J_n(0) = 0$ otherwise, the terms in Eq. (28) evaluated for a collinear superposition of laser and electrons, i.e., $\theta = 0$, reduce to the form:

$$p\langle\ldots\rangle_p|_{\theta=0} = \frac{K}{2\gamma}[JJ] \quad (41)$$

and $[JJ] = J_0(\frac{K^2}{4+2K^2}) - J_1(\frac{K^2}{4+2K^2})$ is the usual coupling constant. This is an intermediate confirmation of the correctness of the above derivation.

The same passages lead (see Appendix B) to similar expressions for the other two terms in Eq. (28):

$$\langle\ldots\rangle_o = J_1^{-2,1}(a,d)$$
$$\langle\ldots\rangle_q = \frac{1}{2}[J_1^{2,1}(a,d) - J_3^{-2,1}(a,d)]. \quad (42)$$

Accordingly, the coupling term introduced in Eq. (24) now reads:

$$\sum_{JJ}(\vartheta) = -\frac{p}{2}[J_0^{-2,1}(a,d) + J_2^{-2,1}(a,d)]$$
$$+\frac{q}{2}[J_1^{2,1}(a,d) - J_3^{-2,1}(a,d)] + o\cdot J_1^{-2,1}(a,d). \quad (43)$$

Since the index n of the infinite series in Eq. (43) also determines the order of the Bessel functions, successive terms of the series will be smaller and smaller in value for higher n. The convergence of the series is, in fact, guaranteed already for $|n| = 4$ (see Appendix B). One should also be reminded that the dependence on the ϑ parameter is hidden in the arguments a, d of the Bessel functions. By dropping the interaction angle to zero, it returns as expected:

$$\sum_{JJ}(0) = \frac{K}{2\gamma}[JJ]. \quad (44)$$

B. Numerical results

Electron beam and laser heater parameters are inspired to [84]. In the absence of dispersive motion, we assume electron and laser beam sizes at the waist in the undulator squeezed to 100 and 150 μm, respectively, see Table IV. The parameters allow beam heating in excess of 30 keV with 0.5 MW peak power for the collinear interaction. The maximum repetition rate assumed hereafter is 1 MHz.

Figure 17 shows the dependence from the interaction angle of the LH-induced rms energy spread at fixed peak power (top), and of the laser peak power at fixed induced energy spread of 30 keV (bottom). Two sets of undulator periods are considered to match the laser wavelength at the fundamental wavelength and at the second harmonic, respectively (see Table IV). The deviation of the series representation [Eq. (43)] and of the integral [Eq. (24)] is negligible for all angles, as also shown in Fig. 18, confirming that our analytical derivation is exact.

At the interaction angle of 3 mrad, the maximum heating level of 30 keV can be obtained with 4 MW peak—50 W average power at the second harmonic of the Yb-Nd laser, or at 1 MW peak—11 W average, for the laser at the fundamental harmonic (1.065 μm). The nominal peak power reported in [85] at the laser second harmonic is 2 MW.

By keeping $\theta = 3$ mrad as the maximum tolerable angle for the laser power, and assuming a vacuum chamber iris

TABLE IV. Laser heater parameters.

Electron bunch			
Mean energy	146		MeV
Normalized emittance, rms	0.6		μm
Betatron function at the waist	5		m
Transverse rms size at the waist	100		μm
Charge	<1		nC
Duration, FWHM	8		ps
LH-induced energy spread, rms	<30		keV
Undulator			
Period length	43		mm
Number of periods	11		
Undulator parameter K	1.43		
Laser pulse			
Central wavelength	532	1064	nm
rms size at the waist (x, y)	150		μm
Duration, FWHM	11		ps
Peak power at $\theta = 0$	<0.50	<0.12	MW
Average power at $\theta = 0$ and 1 MHz RR.	<5.5	<1.5	W

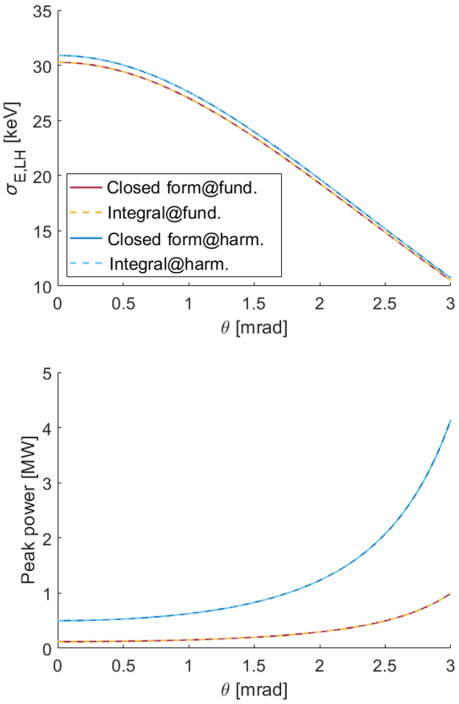

FIG. 17. Laser heater-induced energy spread (top) and laser peak power (bottom) as a function of the interaction angle. The laser heater is at the resonant condition at the fundamental and at the second-harmonic of the IR laser. Series representation and numerical integration superimpose.

radius of ∼10 mm, the laser injection port should be approximately 4 m upstream the undulator. Assuming a laser rms size of 150 μm at waist in the middle of the undulator, the laser spot size at the port would be 230 μm or 170 μm, at the fundamental or at the second harmonic, respectively. Neither the need for special focusing nor interference with the linac layout emerges at this stage.

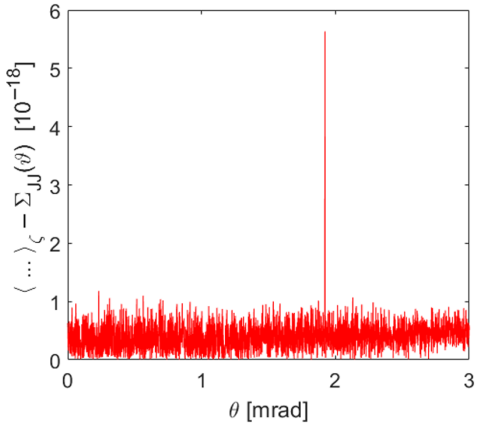

FIG. 18. Numerical deviation of the series representation [Eq. (43)] and of the numerical integration [Eq. (24)], in unit of 10^{-17}, as a function of the interaction angle.

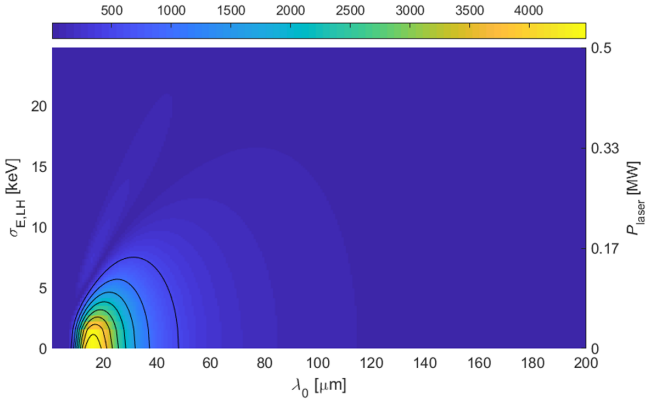

FIG. 19. Contour plot of the spectral gain at the end of the 1.5 GeV, two-stage linac setting (see Table I and Fig. 8) as a function of the laser heater peak power. The induced energy spread is calculated for an interaction angle of 3 mrad.

To make a connection with the aforementioned comparative study, a 2D map of the MBI gain of the 1.5 GeV linac, two-stage compression—whose gain is the largest among all four setups considered so far, see Fig. 8—is produced in Fig. 19. The spectral gain is function of the laser heater peak power at the interaction angle of 3 mrad. The FERMI laser heater parameters are adopted [16]. The feasibility of the oblique interaction is confirmed in this case too.

VI. CONCLUSIONS

A systematic and comprehensive comparison of two semianalytical models (HK and BKW) of microbunching instability in XUV linac-FELs is presented. In concrete, the spectrum of the bunching factor and of the energy modulation amplitude is calculated with a script, following the prescriptions introduced in [26,27]. The instability gain and the beam slice energy spread are derived accordingly.

The original formalisms have been enriched with on-demand features, including low gain terms, second order correction to the linear gain, intrabeam scattering, and arbitrary transverse mismatch of laser and electron beam in the laser heater. The models have been benchmarked for one- and two-stage compression, in a low and high energy accelerator, so covering a wide range of parameters of XUV FELs.

The agreement between the two models is good. The deviation in gain, energy modulation, and slice energy spread is typically smaller than 10% when all collective effects, and primarily CSR and LSC, are included, regardless of the magnitude of the gain or beam heating, and with the same modeling of IBS.

The comparative study suggests the tendency of the HK formalism to predict a larger LSC-driven gain and a smaller CSR-driven one than BKW. This can lead to a different redistribution of gain and energy spread along the line, with the largest local deviation in peak gain of ∼30% for $C > 30$

in one -stage, but reducing to $< 10\%$ in two-stage and total $C \sim 150$, for example. The contribution to the total gain from the dipole exit-transient CSR field in bunch compressors, modeled through CER impedance, is less than 10%.

Numerical results from both models confirm the gain to be independent from the initial bunching, also in the presence of low gain terms and large initial modulation amplitudes. The dependence of the linear and nonlinear (second-order) gain from the initial peak current is in good agreement with the theoretical expectation, i.e., $G^2/G^1 \propto I_0^\alpha$, and $\alpha \cong 1$. Nevertheless, it is found that for the nonlinear gain to become noticeable (say, $> 10\%$ increase of the linear gain and energy spread), the unrealistic scenario of large compression factor and large momentum compaction but in the absence of IBS should be considered.

Three different models of IBS—one of which is introduced anew in Eq. (17)—can lead to peak-to-peak deviation in predicted gain and energy spread at the end of the accelerator as large as ~30% for very large gain ($G^1 > 10^3$). The largest deviation is systematically detected between Eqs. (14) and Eq. (16). The deviation reduces to $< 15\%$ when comparing Eqs. (16) and (17).

The proposed implementations of HK and BKW both allow, within the aforementioned numerical uncertainties and well within the experimental ones, the recovery of agreement of predicted and measured slice energy spread in cases so far never benchmarked with theory [81], in disagreement with theory lacking IBS [39], or in partial agreement by virtue of blind fitting of IBS parameters [40]. In the latter case, the analysis reveals the fundamental contribution of low gain terms to the minimization of the energy spread as a function of the laser heater chicane's R_{56}.

While it was not possible, owing to the available experimental data, to discriminate the degree of reliability of the "closed form" [Eq. (17)] vs the "integral form" of IBS [Eq. (16)]—the two providing the same prediction for the experimental set of parameters under study—it emerges that IBS modeled by "constant Clog" [Eq. (14)] tends to overestimate the induced energy spread, hence the effect of longitudinal Landau damping.

The observed interaction of the laser heater chicane with the development of MBI at low energy suggests a scheme in which beam heating is implemented without a chicane. An approximated series representation for the energy spread induced by an obliquely incident laser is found and successfully compared to the numerical integration introduced in [86]. The study shows the feasibility of the oblique interaction in suppressing the instability for incident angles up to a few mrad. In this case, the oblique interaction would save some meters of space along the linac axis, at the expense of a laser power twofold to threefold larger than in collinear laser-electrons geometry. Despite the power increase, up to ~30 keV rms energy spread can be induced at beam energies < 200 MeV by an IR laser average power < 50 W, up to MHz repetition rate.

We conclude that, despite several approximations and effective beam models, the presented implementations of HK and BKW formalism are equivalently capable of capturing the salient MBI physics in a wide range of operational parameters of XUV FELs. While the absolute numerical accuracy of the predicted gain and energy spread certainly depends, for example, on the accuracy of the experimental data for the beam parameters at the injector exit and the beam optics along the line, the models are well suited for a global optimization of the linac setting in the presence of MBI. In general, the inclusion of low gain terms and of IBS according to Eq. (16) or (17) is recommended.

From a general perspective, we judge the BKW matrix formalism better suited to the inclusion of new impedances and to the modeling of magnetic dispersive insertions of arbitrary geometry. At the same time, the BKW allows neither to turn low gain terms off, unless the architecture of the model is profoundly revised, nor to inspect the instability strength at intermediate points of the beamline, unless a sufficiently dense definition of matrices is introduced to describe the accelerator. Thus, we expect the choice of one or the other model to be primarily guided by the specific configuration of the beamline under study.

ACKNOWLEDGMENTS

The FERMI team is acknowledged for insightful discussions. G. C. acknowledges the University of Rome La Sapienza–Department of Physics and INFN–LNF for financial support. S. D. M. acknowledges Demin Zhou for insights on the LSC impedance and Agostino Marinelli for suggestions to the derivation in Appendix A.

APPENDIX A: MICROBUNCHING-INDUCED ENERGY SPREAD

Let us assume a longitudinal charge distribution function $\rho(z)$ described by means of the Heaviside step function $H(z)$, and whose duration Δz_b is much longer than any modulation wavelength λ under consideration. The amplitude of the distribution function is such that

$$\int_{-\infty}^{+\infty} \rho(z)dz = \frac{1}{\sigma_z}\int_{-\infty}^{+\infty}[H(z) - H(z-\sigma_z)]dz = 1. \quad \text{(A1)}$$

If $\Delta\gamma(k)/\gamma$ is the energy modulation amplitude relative to the final beam energy γ (in units of electron rest mass), generated by the coupling of the bunching factor $b(k)$ to the path length-integrated impedance $Z_{\text{int}}(k)$ at wavenumber k [see Eq. (6)], its anti-Fourier transform results:

$$\frac{|\Delta\gamma(z)|^2}{\gamma^2} = \left|\sum_{m=-\infty}^{+\infty} b_0(m)G(m)Z_{\text{int}}(m)e^{imkz}\right|^2$$
$$= \sum_m b_0(m)G(m)Z_{\text{int}}(m)e^{imkz}\sum_j b_0^*(j)G(j)Z_{\text{int}}^*(j)e^{-ijkz}$$
$$= \sum_{m=j}\sum_j |b_0(m)G(m)Z_{\text{int}}(m)|^2 + \sum_{m\neq j}\sum_j b_0(m)b_0^*(j)G(m)G(j)Z_{\text{int}}(m)Z_{\text{int}}^*(j)e^{i(m-j)kz}, \quad \text{(A2)}$$

where it is intended:

$$|Z_{\text{int}}(k)| = \left|\frac{4\pi}{Z_0}\frac{I}{I_A}\int_0^s \frac{Z_{\text{coll}}(k;s')}{\gamma(s')}ds'\right| \quad \text{(A3)}$$

and Z_{coll} is the impedance of the beam collective effect per unit length. The equivalent rms energy spread is

$$\frac{\sigma_\gamma^2}{\gamma^2} = \frac{1}{\int_{-\infty}^{+\infty}\rho(z)dz}\int_{-\infty}^{+\infty} dz\frac{|\Delta\gamma(z)|^2}{\gamma^2}\rho(z)$$
$$= \int_{-\infty}^{+\infty} dz\sum_m |b_0(m)G(m)Z_{\text{int}}(m)|^2\rho(z) + \int dz\sum_{m\neq j}\sum_j b_0(m)b_0^*(j)G(m)G(j)Z_{\text{int}}(m)Z_{\text{int}}^*(j)e^{i(m-j)kz}\rho(z). \quad \text{(A4)}$$

In the second addendum of Eq. (A4), $e^{i(m-j)kz}{}_z \approx 0$, and the equation is now brought to continuum, passing from summation to integration over all frequencies, by making use of $\langle|b_0^2(k)|\rangle_z = 1/N_e$, to eventually get

$$\frac{\sigma_\gamma^2}{\gamma^2} = \frac{1}{N_e}\sum_j |G(j)Z_{\text{int}}(j)|^2 = \frac{1}{N_e\Delta k}\sum_j |G(j)Z_{\text{int}}(j)|^2\Delta k$$
$$\to \frac{\sigma_z}{2\pi N_e}\int_{-\infty}^{+\infty} dk|G(k)Z_{\text{int}}(k)|^2$$
$$= \frac{2ec}{I_0}\int_0^{+\infty} \mathrm{d}\lambda\frac{|\mathrm{G}(2\pi/\lambda)Z_{\text{int}}(2\pi/\lambda)|^2}{\lambda^2}, \quad \text{(A5)}$$

and where we used $\Delta k = 2\pi/\sigma_z$, $\mathrm{I}_0 = N_e ec/\sigma_z$, and the limit is taken for $\Delta k \to 0$. Equation (A5) is the result in Eq. (11) and consistent with Eq. (H2) in [39].

APPENDIX B: LASER HEATER-INDUCED ENERGY SPREAD

It is shown below the full derivation of the quantities reported in Eq. (42). Starting from $\ldots_o$ in Euler notation:

$$\langle\ldots\rangle_o = \frac{1}{2i}(\langle s\rangle - \langle g\rangle)$$
$$= \frac{1}{4\pi i}\left(\int_0^{2\pi} d\varsigma e^{-i\varsigma}e^{ia\sin(2\varsigma)}e^{id\cos(\varsigma)} + \right.$$
$$\left. - \int_0^{2\pi} d\varsigma e^{i\varsigma}e^{-ia\sin(2\varsigma)}e^{-id\cos(\varsigma)}\right) \quad \text{(B1)}$$

we rely again on the Jacobi-Anger expansion in Euler form, together with the definition of the multivariate generalized Bessel function, to compute the terms s, g:

$$\langle s\rangle = \frac{1}{2\pi}\int_0^{2\pi} d\varsigma\, e^{-i\varsigma}e^{ia\sin(2\varsigma)}e^{id\cos(\varsigma)}$$
$$= \frac{1}{2\pi}\int_0^{2\pi} d\varsigma\, e^{-i\varsigma}\left[\sum_{n=-\infty}^{\infty} J_n(a)e^{2in\varsigma}\right]\left[\sum_{m=-\infty}^{\infty}(i)^m J_m(d)e^{im\varsigma}\right]$$
$$= \frac{1}{2\pi}\sum_{n=-\infty}^{\infty} J_n(a)\sum_{m=-\infty}^{\infty}(i)^m J_m(d)\int_0^{2\pi} d\varsigma\, e^{i\varsigma(2n+m-1)}$$
$$= \sum_{n=-\infty}^{\infty}\sum_{m=-\infty}^{\infty}(i)^m J_m(d)J_n(a)\delta_{(2n+m-1),0}$$
$$= \sum_{n=-\infty}^{\infty}(i)^{1-2n}J_n(a)J_{1-2n}(d)$$
$$= i\sum_{n=-\infty}^{\infty} J_{-n}(a)J_{1-2n}(d) = iJ_1^{-2,1}(a,d);$$

$$\begin{aligned}\langle g\rangle &= \frac{1}{2\pi}\int_0^{2\pi} d\varsigma\, e^{i\varsigma} e^{-ia\sin(2\varsigma)} e^{-id\cos(\varsigma)} \\ &= \frac{1}{2\pi}\int_0^{2\pi} d\varsigma\, e^{i\varsigma}\left[\sum_{n=-\infty}^{\infty} J_n(a) e^{-2in\varsigma}\right]\left[\sum_{m=-\infty}^{\infty} (-i)^m J_m(d) e^{im\varsigma}\right] \\ &= \frac{1}{2\pi}\sum_{n=-\infty}^{\infty} J_n(a)\sum_{m=-\infty}^{\infty} (-i)^m J_m(d)\int_0^{2\pi} d\varsigma\, e^{i\varsigma(-2n+m+1)} \\ &= \sum_{n=-\infty}^{\infty}\sum_{m=-\infty}^{\infty} (-i)^m J_m(d) J_n(a)\delta_{(-2n+m+1),0} \\ &= \sum_{n=-\infty}^{\infty} (-i)^{2n-1} J_n(a) J_{2n-1}(d) \\ &= \frac{1}{i}\sum_{n=-\infty}^{\infty} J_{-n}(a) J_{1-2n}(d) = -iJ_1^{-2,1}(a,d). \end{aligned} \tag{B2}$$

Making use of Eq. (B2):

$$\begin{aligned}\langle\ldots\rangle_o &= \frac{1}{2i}[\langle s\rangle - \langle g\rangle] = \frac{1}{2i}[\mathrm{i}J_1^{-2,1}(a,d) + iJ_1^{-2,1}(a,d)] \\ &= J_1^{-2,1}(a,d), \end{aligned} \tag{B3}$$

as reported in Eq. (42). The analogous derivation is conducted to retrieve the $\langle\ldots\rangle_q$ quantity in terms of Bessel functions:

$$\begin{aligned}\langle\ldots\rangle_q &= \frac{1}{4i}\langle e^{i\varsigma} e^{ia\sin(2\varsigma)} e^{id\cos(\varsigma)} - e^{3i\varsigma} e^{-ia\sin(2\varsigma)} e^{-id\cos(\varsigma)} \\ &\quad + cc\rangle_\varsigma \equiv \frac{1}{4i}[(\langle h\rangle - \langle f\rangle) + (\langle f^*\rangle - \langle h^*\rangle)]. \end{aligned} \tag{B4}$$

It can be shown that $\langle h^*\rangle = \langle -h\rangle$ and $\langle f^*\rangle = \langle -f\rangle$ so that Eq. (B4) reduces to

$$\langle\ldots\rangle_q = \frac{1}{2i}[(\langle h\rangle - \langle f\rangle)]. \tag{B5}$$

The evaluation of $\langle h\rangle, \langle f\rangle$ leads to

$$\begin{aligned}\langle h\rangle &= \frac{1}{2\pi}\int_0^{2\pi} d\varsigma\, e^{i\varsigma} e^{ia\sin(2\varsigma)} e^{id\cos(\varsigma)} \\ &= \frac{1}{2\pi}\int_0^{2\pi} d\varsigma\, e^{i\varsigma}\left[\sum_{n=-\infty}^{\infty} J_n(a) e^{2in\varsigma}\right]\left[\sum_{m=-\infty}^{\infty} (i)^m J_m(d) e^{im\varsigma}\right] = \frac{1}{2\pi}\sum_{n=-\infty}^{\infty} J_n(a)\sum_{m=-\infty}^{\infty} (i)^m J_m(d)\int_0^{2\pi} d\varsigma\, e^{i\varsigma(2n+m+1)} \\ &= \sum_{n=-\infty}^{\infty}\sum_{m=-\infty}^{\infty} (i)^m J_m(d) J_n(a)\delta_{(2n+m+1),0} \\ &= \sum_{n=-\infty}^{\infty} (i)^{-1-2n} J_n(a) J_{-1-2n}(d) \\ &= \frac{1}{i}\sum_{n=-\infty}^{\infty} J_{-n}(a) J_{1-2n}(d) = i\, J_1^{2,1}(a,d); \end{aligned}$$

$$\begin{aligned}\langle f\rangle &= \frac{1}{2\pi}\int_0^{2\pi} d\varsigma\, e^{3i\varsigma} e^{-ia\sin(2\varsigma)} e^{-id\cos(\varsigma)} \\ &= \frac{1}{2\pi}\int_0^{2\pi} d\varsigma\, e^{3i\varsigma}\left[\sum_{n=-\infty}^{\infty} J_n(a) e^{-2in\varsigma}\right]\left[\sum_{m=-\infty}^{\infty} (-i)^m J_m(d) e^{im\varsigma}\right] \\ &= \frac{1}{2\pi}\sum_{n=-\infty}^{\infty} J_n(a)\sum_{m=-\infty}^{\infty}(-i)^m J_m(d)\int_0^{2\pi} d\varsigma\, e^{i\varsigma(-2n+m+3)} \\ &= \sum_{n=-\infty}^{\infty}\sum_{m=-\infty}^{\infty}(-i)^m J_m(d) J_n(a)\delta_{(-2n+m+3),0} \\ &= \sum_{n=-\infty}^{\infty}(-i)^{2n-3} J_n(a) J_{2n-3}(d) \\ &= -\frac{1}{i}\sum_{n=-\infty}^{\infty} J_{-n}(a) J_{3-2n}(d) = i\, J_3^{-2,1}(a,d). \end{aligned} \tag{B6}$$

Equation (B5) now reads

$$\begin{aligned}\langle\ldots\rangle_q &= \frac{1}{2i}[\langle h\rangle - \langle f\rangle] = \frac{1}{2i}[\mathrm{i}J_1^{2,1}(a,d) - iJ_3^{-2,1}(a,d)] \\ &= \frac{1}{2}[J_1^{2,1}(a,d) - J_3^{-2,1}(a,d)]. \end{aligned} \tag{B7}$$

In summary, Eqs. (B3), (B7), and (40) allow Eq. (28) to be cast in the following form:

$$\begin{aligned} o\langle\ldots\rangle_o &= o\cdot J_1^{-2,1}(a,d) \\ p\langle\ldots\rangle_p &= -\frac{p}{2}[J_0^{-2,1}(a,d) + J_2^{-2,1}(a,d)] \\ q\langle\ldots\rangle_q &= \frac{q}{2}[J_1^{2,1}(a,d) - J_3^{-2,1}(a,d)]. \end{aligned} \tag{B8}$$

The coupling factor introduced in Eq. (24) eventually reads

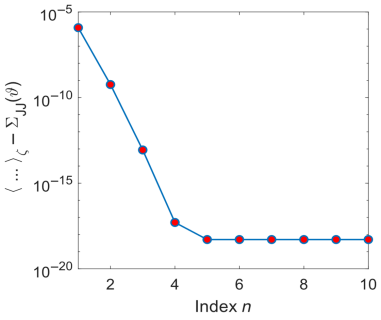

FIG. 20. Convergence of the series representation to the original integral expression in [86], as a function of the series index n.

$$\begin{aligned}\sum_{JJ}(\vartheta) = &-\frac{p}{2}\cdot[J_0^{-2,1}(a,d) + J_2^{-2,1}(a,d)] \\ &+\frac{q}{2}\cdot[J_1^{2,1}(a,d) - J_3^{-2,1}(a,d)] + o\cdot J_1^{-2,1}(a,d). \end{aligned} \tag{B9}$$

The convergence of the series in Eq. (B9) to the original integral expression in [86], as a function of the index n, is shown in Fig. 20.

[1] Z. Huang and G. Stupakov, Control and application of beam microbunching in high brightness linac-driven free electron lasers, Nucl. Instrum. Methods Phys. Res., Sect. A **907**, 182 (2018).

[2] G. Marcus, W. M. Fawley, D. Bohler, Y. Ding, Y. Feng, E. Hemsing, Z. Huang, J. Krzywinski, A. Lutman, and D. Ratner, Experimental observations of seed growth and accompanying pedestal contamination in a self-seeded, soft x-ray free-electron laser, Phys. Rev. Accel. Beams **22**, 080702 (2019).

[3] P. Rebernik Ribic *et al.*, Coherent soft X-ray pulses from an echo-enabled harmonic generation free-electron laser, Nat. Photonics **13**, 555 (2019).

[4] N. S. Mirian *et al.*, Characterization of soft x-ray echo-enabled harmonic generation free-electron laser pulses in the presence of incoherent electron beam energy modulations, Phys. Rev. Accel. Beams **24**, 080702 (2021).

[5] J. Wu, P. Emma, Z. Huang, C. Limborg, and M. Borland, Temporal profile of the LCLS photocathode ultraviolet drive laser tolerated by the microbunching instability, in *Proceedings of the International LINAC Conference 2004, TUP53, Lübeck, German* (2004). Also SLAC-PUB-10430 and LCLS-TN-04-6 (2004).

[6] S. Bettoni, M. Csatari Divall, R. Ganter, M. Pedrozzi, E. Prat, S. Reiche, T. Schietinger, A. Trisorio, C. Vicario, and V. Goryashko, Impact of laser stacking and photocathode

materials on microbunching instability in photoinjectors, Phys. Rev. Accel. Beams **23**, 024401 (2020).
[7] M. Hüning, Ph. Piot, and H. Schlarb, Observation of longitudinal phase space fragmentation at the TESLA test facility free-electron laser, Nucl. Instrum. Methods Phys. Res., Sect. A **475**, 348 (2001).
[8] E. L. Saldin, E. A. Schneidmiller, and M. V. Yurkov, Klystron instability of a relativistic electron beam in a bunch compressor, Nucl. Instrum. Methods Phys. Res., Sect. A **490**, 1 (2002).
[9] J. Rosenzweig, C. Pellegrini, L. Serafini, C. Ternieden, and G. Travish, Space-charge oscillations in a self-modulated electron beam in multi-undulator free-electron lasers, Nucl. Instrum. Methods Phys. Res., Sect. A **393**, 376 (1997).
[10] S. Di Mitri, Bunch length compressors, in *Proceedings of the CAS–CERN Accelerator School: Free Electron Lasers and Energy Recovery Linacs, Hamburg, Germany. 2016*, edited by R. Bailey (CERN, Geneva, 2018), and references therein, CERN Yellow Reports: School Proceedings, Report No. CERN-2018-001-SP, Vol. 1/2018.
[11] M. Borland *et al.*, Start-to-end simulation of self-amplified spontaneous emission free electron lasers from the gun through the undulator, Nucl. Instrum. Methods Phys. Res., Sect. A **483**, 268 (2002).
[12] J. Qiang, C. E. Mitchell, and M. Venturini, Suppression of microbunching instability using bending magnets in free-electron-laser linacs, Phys. Rev. Lett. **111**, 054801 (2013).
[13] A. D. Brynes *et al.*, Mitigation of the microbunching instability through transverse Landau damping, Phys. Rev. Accel. Beams **27**, 074402 (2024).
[14] E. L. Saldin, E. A. Schneidmiller, and M. V. Yurkov, Longitudinal space charge-driven microbunching instability in the TESLA Test Facility linac, Nucl. Instrum. Methods Phys. Res., Sect. A **528**, 355 (2004).
[15] Z. Huang *et al.*, Measurements of the Linac Coherent Light Source laser heater and its impact on the x-ray free electron laser performance, Phys. Rev. ST Accel. Beams **13**, 020703 (2010).
[16] S. Spampinati *et al.*, Laser heater commissioning at an externally seeded free-electron laser, Phys. Rev. ST Accel. Beams **17**, 120705 (2014).
[17] S. Di Mitri and S. Spampinati, Microbunching instability suppression via electron-magnetic-phase mixing, Phys. Rev. Lett. **112**, 134802 (2014).
[18] S. Di Mitri, G. Perosa, A. D. Brynes, I. Setija, S. Spampinati, P. H. Williams, A. Wolski, E. Allaria, S. Brussard, L. Giannessi, G. Penco, P. R. Rebernik, and M. Trovò, Experimental evidence of intrabeam scattering in a free-electron laser driver, New J. Phys. **22**, 083053 (2020).
[19] G. Bassi, J. A. Ellison, and R. Warnock, Vlasov treatment of coherent synchrotron radiation from arbitrary planar orbits, Nucl. Instrum. Methods Phys. Res., Sect. A **558**, 85 (2006).
[20] M. Dohlus and T. Limberg, in *Proceedings of the 26th International Free Electron Laser Conference, Trieste, Italy* (Comitato Conferenze Elettra, Trieste, Italy, 2004), MOCOS05.
[21] Ji Qiang, Y. Ding, P. Emma, Z. Huang, D. Ratner, T. O. Raubenheimer, M. Venturini, and F. Zhou, Start-to-end simulation of the shot-noise driven microbunching instability experiment at the Linac Coherent Light Source, Phys. Rev. Accel. Beams **20**, 054402 (2017).
[22] M. Borland, Modelling of the microbunching instability, Phys. Rev. ST Accel. Beams **11**, 030701 (2008).
[23] M. Venturini, Microbunching instability in single-pass systems using a direct two-dimensional Vlasov solver, Phys. Rev. ST Accel. Beams **10**, 104401 (2007).
[24] M. Migliorati, G. Dattoli, A. Schiavi, and M. Venturini, A Vlasov solver for collective effects in particle accelerators, Il Nuovo Cimento **32**, 2 (2009).
[25] C.-Y. Tsai, D. Douglas, R. Li, and C. Tennant, Linear microbunching analysis for recirculation machines, Phys. Rev. Accel. Beams **19**, 114401 (2016).
[26] Z. Huang and K.-J. Kim, Formulas for coherent synchrotron radiation microbunching in a bunch compressor chicane, Phys. Rev. ST Accel. Beams **5**, 074401 (2002).
[27] R. A. Bosch, K. J. Kleman, and J. Wu, Modeling two-stage bunch compression with wakefields: Macroscopic properties and microbunching instability, Phys. Rev. ST Accel. Beams **11**, 090702 (2008).
[28] A. Marinelli, E. Hemsing, and J. Rosenzweig, Three-dimensional analysis of longitudinal plasma oscillations in a thermal relativistic electron beam, Phys. Plasmas **18**, 103105 (2011).
[29] V. N. Litvinenko *et al.*, Plasma-cascade instability, Phys. Rev. Accel. Beams **24**, 014402 (2021).
[30] J. Wu, Z. Huang, and P. Emma, Analytical analysis of longitudinal space charge effects for a bunched beam with radial dependence, Phys. Rev. ST Accel. Beams **11**, 040701 (2008).
[31] Marco Venturini, Models of longitudinal space-charge impedance for microbunching instability, Phys. Rev. ST Accel. Beams **11**, 034401 (2008).
[32] M. Veturini, R. Warnock, and A. Zholents, Vlasov solver for longitudinal dynamics in beam delivery systems for x-ray free electron lasers, Phys. Rev. ST Accel. Beams **10**, 054403 (2007).
[33] M. Venturini and A. Zholents, Modeling microbunching form shot noise using Vlasov solvers, Nucl. Instrum. Methods Phys. Res., Sect. A **593**, 53 (2008).
[34] M. Veturini, M. Migliorati, C. Ronsivalle, M. Ferrario, and C. Vaccarezza, Dynamics of longitudinal phase-space modulations in an rf compressor for electron beam, Phys. Rev. ST Accel. Beams **13**, 080703 (2010).
[35] S. Seletskiy, B. Podobedov, Y. Shen, and X. Yang, Seeding, controlling, and benefiting from the microbunching instability, Phys. Rev. Lett. **111**, 034803 (2013).
[36] Z. Huang, M. Borland, P. Emma, J. Wu, C. Limborg, G. Stupakov, and J. Welch, Suppression of microbunching instability in the linac coherent light source, Phys. Rev. ST Accel. Beams **7**, 074401 (2004).
[37] G. Dattoli, M. Migliorati, and A. Schiavi, Laser heater and coherent synchrotron radiation: Analytical and numerical results, in *Proceedings of the 23rd Particle Accelerator Conference*, Vancouver, Canada, 2009 (IEEE, Piscataway, NJ, 2009), TU5RFP063.
[38] J. Qiang, J. Corlett, P. Emma, C. E. Mitchell, and M. Venturini, Simulation and analysis of microbunching instability in a high repetition rate FEL beam delivery

system, in *Proceedings of the 4th International Particle Accelerator Conference, IPAC-2013, Shanghai, China* (JACoW, CERN, Geneva, Switzerland, 2013), TUPME062, pp. 1709–1711.

[39] D. Ratner, C. Behrens, Y. Ding, Z. Huang, A. Marinelli, T. Maxwell, and F. Zhou, Time-resolved imaging of the microbunching instability and energy spread at the Linac Coherent Light Source, Phys. Rev. ST Accel. Beams **18**, 030704 (2015).

[40] E. Prat, P. Craievich, P. Dijkstal, S. Di Mitri, E. Ferrari, T. G. Lucas, A. Malyzhenkov, G. Perosa, S. Reiche, and T. Schietinger, Energy spread blowup by intrabeam scattering and microbunching at the SwissFEL injector, Phys. Rev. Accel. Beams **25**, 104401 (2022).

[41] W. Cheng, Y. Gong, M. Zhao, M. Zhang, and D. Gu, Inhibition of microbunching instability in the Shanghai soft x-ray free-electron laser user facility, Nucl. Instrum. Methods Phys. Res., Sect. A **1050**, 168145 (2023).

[42] A. D. Brynes *et al.*, Microbunching instability characterization via temporally modulated laser pulses, Phys. Rev. Accel. Beams **23**, 104401 (2020).

[43] E. Allaria *et al.*, Highly coherent and stable pulses from the FERMI seeded free-electron laser in the extreme ultraviolet, Nat. Photonics **6**, 699 (2012).

[44] B. Liu *et al.*, Demonstration of a widely-tunable and fully-coherent high-gain harmonic-generation free-electron laser, Phys. Rev. Accel. Beams **16**, 020704 (2013).

[45] W. Ackermann *et al.*, Generation of Coherent 19- and 38-nm Radiation at a Free-Electron Laser Directly Seeded at 38 nm, Phys. Rev. Lett. **111**, 114801 (2013).

[46] A. M. Kondratenko and E. L. Saldin, Generation of coherent radiation by a relativistic electron beam in an undulator, Part. Accel. **10**, 207 (1980), 0031-2460/80/1003-0207 $06.50/0.

[47] R. Bonifacio, C. Pellegrini, and L. Narducci, Collective instabilities and high-gain regime in a free electron laser, Opt. Commun. **50**, 373 (1984).

[48] P. Emma *et al.*, First lasing and operation of an ångstrom-wavelength free-electron laser, Nat. Photonics **4**, 641 (2010).

[49] T. Ishikawa *et al.*, A compact X-ray free-electron laser emitting in the sub-ångström region, Nat. Photonics **6**, 540 (2010).

[50] H.-S. Kang *et al.*, Hard X-ray free-electron laser with femtosecond-scale timing jitter, Nat. Photonics **11**, 708 (2017).

[51] M. Venturini, An effective longitudinal space-charge impedance model for beams with non-uniform and non-axis-symmetric transverse density, Report No. LBNL-63111, 2007 10.2172/927331; See also J. Qiang, R. D. Ryne, M. Venturini, A. A. Zholents, and I. V. Pogorelov, High resolution simulation of beam dynamics in electron linacs for x-ray free electron lasers, Phys. Rev. ST Accel. Beams **12**, 100702 (2009).

[52] D. Zhou and N. Yie, Wake fields and impedance of space charge in Cartesian coordinate system, arXiv:2101.04369v1.

[53] Y. Li and L. Wang, Approximate longitudinal space charge impedances of a round beam between parallel plates, and inside a rectangular chamber, Nucl. Instrum. Methods Phys. Res., Sect. A **769**, 44 (2015).

[54] J. B. Murphy, S. Krinsky, and R. Gluckstern, Longitudinal Wakefield for Synchrotron Radiation, in *Proceedings of the Particle Accelerator Conference, Dallas, TX, 1995* (IEEE, New York, 1995), p. 2980.

[55] R. Li, C. L. Bohn, and J. J. Bisognano, Analysis on the steady-state coherent synchrotron radiation with strong shielding, in *Proceedings of the Particle Accelerator Conference, Vancouver, BC, Canada, 1997* (IEEE, New York, 1997), p. 1644.

[56] T. Agoh, Steady fields of coherent synchrotron radiation in a rectangular pipe, Phys. Rev. ST Accel. Beams **12**, 094402 (2009).

[57] Ya. S. Derbenev, J. Rossbach, E. L. Saldin, and V. D. Shiltsev, Microbunch radiative tail-head interaction, DESY, Hamburg, Germany, Report No. TESLA-FEL 95-05, 1995.

[58] A. D. Brynes *et al.*, Beyond the limits of 1D coherent synchrotron radiation, New J. Phys. **20**, 073035 (2018); **23**, 049401(A) (2021).

[59] E. L. Saldin, E. A. Schneidmiller, and M. V. Yurkov, On the coherent radiation of an electron bunch moving in an arc of a circle, Nucl. Instrum. Methods Phys. Res., Sect. A **398**, 373 (1997).

[60] P. Emma and G. Stupakov, CSR wake for a short magnet in ultrarelativistic limit, in *Proceedings of the 8th European Accelerator Conference, Paris, 2002, Genoa, Italy* (EPS-IGA and CERN, Geneva, 2002), WEPRI029, p. 1479.

[61] S. Di Mitri, Feasibility study of a periodic arc compressor in the presence of coherent synchrotron radiation, Nucl. Instrum. Methods Phys. Res., Sect. A **806**, 184 (2016).

[62] B. Liu, C.-Y. Tsai, Y. Jiao, W. Liu, F. Zeng, and W. Qin, Analytical formulas of coherent synchrotron radiation induced microbunching gain and emittance growth in an arbitrary achromatic four-bend chicane, Nucl. Instrum. Methods Phys. Res., Sect. A **1067**, 169703 (2016).

[63] R. A. Bosch, Longitudinal wake of a bunch of suddenly accelerated electrons within the radiation formation zone, Phys. Rev. ST Accel. Beams **10**, 050701 (2007).

[64] G. Stupakov, Centripetal transverse wakefield in relativistic beam, arXiv:1901.10745.

[65] T. O. Raubenheimer, P. Emma, and S. Kheifets, Chicane and Wiggler based bunch compressors for Future Linear Colliders, in *Proceedings of the 15th Particle Accelerator Conference, PAC-1993, Washington, DC, 1993* (IEEE, New York, 1993), pp. 635–637.

[66] D. Ratner, Z. Huang, and G. Stupakov, Analysis of shot noise suppression for electron beams, Phys. Rev. ST Accel. Beams **14**, 060701 (2011); See also D. Ratner, Ph.D. thesis, Much ado about microbunching: Coherent bunching in high brightness electron beams, Report No. SLAC-R-992, 2011, https://www.slac.stanford.edu/pubs/slacreports/reports19/slac-r-992.pdf.

[67] D. Ratner, Z. Huang, and G. Stupakov, Observation of shot noise suppression at optical wavelengths in a relativistic electron beam, Phys. Rev. Lett. **109**, 034801 (2012).

[68] A. Gover, A. Nause, E. Dyunin, and M. Fedurin, Beating the shot-noise limit, Nat. Phys. **8**, 877 (2012).

[69] M. Venturini, Shot-noise seeded microbunching instability: Second-order correction to the gain function, Nucl. Instrum. Methods Phys. Res., Sect. A **599**, 140 (2009).

[70] A. Piwinski, Intra-beam scattering, in *Proceedings of the 9th International Conference on High Energy Accelerators* (1974), p. 405, 10.5170/CERN-1992-001.226.

[71] J. D. Bjorken and S. K. Mtingwa, Intrabeam scattering, Part. Accel. **13**, 115 (1983), FERMILAB-PUB-82/47-THY.

[72] K. L. F. Bane, An accurate, simplified model of intrabeam scattering, Report No. SLAC-AP-141 2002, also in arXiv: physics/0205058.

[73] Z. Huang, Intrabeam scattering in an X-ray FEL driver, Stanford Linear Accelerator Center, Stanford University, Stanford, CA, Report No. LCLS-TN-02-8, 2002.

[74] T. O. Raubenheimer, The core emittance with intrabeam scattering in e^+/e^- rings, Part. Accel. **45**, 111 (1994), SLAC-PUB-5790.

[75] S. Di Mitri, G. Perosa, A. D. Brynes, I. Setija, S. Spampinati, P. H. Williams, A. Wolski, E. Allaria, S. Brussard, L. Giannessi, G. Penco, P. R. Rebernik, and M. Trovò, Addendum: Experimental evidence of intrabeam scattering in a free-electron laser driver, New J. Phys. **24**, 039401 (2022).

[76] G. Perosa and S. Di Mitri, Matrix model for collective phenomena in electron beam's longitudinal phase space, Sci. Rep. **11**, 7895 (2021).

[77] S. Heifets, G. Stupakov, and S. Krinsky, Coherent synchrotron radiation instability in a bunch compressor, Phys. Rev. ST Accel. Beams **5**, 064401 (2002).

[78] J. Tang *et al.*, Laguerre-Gaussian mode laser heater for microbunching instability suppression in free-electron lasers, Phys. Rev. Lett. **124**, 134801 (2020).

[79] E. Ferrari, E. Allaria, W. Fawley, L. Giannessi, Z. Huang, G. Penco, and S. Spampinati, Impact of non-Gaussian electron energy heating upon the performance of a seeded free-electron laser, Phys. Rev. Lett. **112**, 114802 (2014).

[80] J.-W. Park, Y. Kim, and Y. W. Parc, Dependency of a compact and analytical gain function for the linac with multiple bunch compressors on the initial density modulation, Nucl. Instrum. Methods Phys. Res., Sect. A **999**, 165226 (2021).

[81] G. Penco, G. Perosa, E. Allaria, S. Di Mitri, E. Ferrari, L. Giannessi, S. Spampinati, C. Spezzani, and M. Veronese, Enhanced seeded free electron laser performance with a "cold" electron beam, Phys. Rev. Accel. Beams **23**, 120704 (2020).

[82] S. Di Mitri and S. Spampinati, Microbunching instability study in a linac-driven free electron laser spreader beam line, Phys. Rev. Accel. Beams **20**, 120701 (2017).

[83] G. Perosa *et al.*, Linear optics control of sideband instability for improved free-electron laser spectral brightness, Phys. Rev. Accel. Beams **23**, 110703 (2020).

[84] C. Gerth *et al.*, Layout of the laser heater for FLASH2020+, in *Proceedings of the 12th International Particle Accelerator Conference, IPAC-2021, Campinas, Brazil* (JACoW, Geneva, Switzerland, 2021), TUPAB111, pp. 1647–1650, 10.18429/JACoW-IPAC2021-TUPAB111.

[85] C. Gerth *et al.*, First beam heating with the laser heater for FLASH2020+, in *Proceedings of the 14th International Particle Accelerator Conference, IPAC-2023, Venice, Italy* (JACoW, Geneva, Switzerland, 2023), TUPL098, pp. 1950–1953.

[86] X. Wang, C. Feng, C.-Y. Tsai, L. Zeng, and Z. Zhao, Obliquely incident laser and electron beam interaction in an undulator, Phys. Rev. Accel. Beams **22**, 070701 (2019).

[87] S. Di Mitri, W. Barletta, A. Bianco, I. Cudin, B. Diviacco, L. Raimondi, S. Spampinati, C. Spezzani, and C. Masciovecchio, Laser-slicing at a low-emittance storage ring, J. Synchrotron Radiat. **26**, 1523 (2019).